NA62 Collaboration
26.03.2015

2015 NA62 Status Report to the CERN SPSC

Abstract

NA62 aims to study the rare decay $K^+ \to \pi^+\nu\bar{\nu}$ at the CERN SPS. In this document we report the status of the detector construction and the general progress of the experiment since April 2014. Most major detectors were complete and installed. The commissioning of the experiment took place during the October - December 2014 SPS run and we report here extensively on a first look at the data. The status of the preparation and the prospects for the 2015 run are presented.

Contents

1 Introduction **2**

2 Technical Co-ordination **3**

3 Beam **7**

4 KTAG **9**
4.1 Front-end Electronics 10
4.2 Detector Control System (DCS) 10
4.3 2014 Data Taking 11

5 GigaTracKer (GTK) **12**
5.1 Introduction 12
5.2 ASIC chip characterization 12
5.3 Bump-bonding 13
5.4 GTK carrier 14
5.5 Mechanical integration with Micro-channel cooling plates 16
5.6 Mechanical Integration with Vessel 18
5.7 Cooling Plant 18
5.8 DAQ Status 19
5.9 Run 2014 20
5.10 GTK Data 22

6 CHANTI **24**
6.1 Construction and tests 24
6.2 Front End Electronics and calibrations 25
6.3 CHANTI in year 2014 run 26

7 Straw Tracker **27**

CERN-SPSC-2015-012 / SPSC-SR-157
26/03/2015

8 RICH **27**
8.1 RICH vessel . . . 28
8.2 Mirrors system . . . 28
8.3 PMT and readout electronics . . . 30
8.4 RICH commissioning and preliminary results . . . 30

9 Photon Vetos **32**
9.1 LAV . . . 32
9.2 LAV performance studies . . . 34
9.3 SAC and IRC . . . 37

10 CHOD **39**

11 LKr **40**
11.1 Installation of the new readout . . . 40

12 LKr trigger system **42**
12.1 Performance and tests . . . 43
12.2 Production and installation . . . 44

13 Muon Veto System (MUV) **45**
13.1 MUV1 Detector . . . 46
13.2 MUV2 Detector . . . 46
13.3 MUV3 Detector . . . 47

14 Trigger and Data Acquisition **47**
14.1 Common infrastructure . . . 48
14.2 Common TDC-based TDAQ system . . . 48
14.3 Online farm . . . 49
14.4 Trigger system . . . 50
14.5 Conclusions . . . 51

15 First Look at the 2014 data **51**
15.1 Single Track Analysis . . . 52
15.2 Selection of the main decay modes . . . 58

16 Publications and analysis of older data **59**

1 Introduction

NA62 [1] is devoted to the exploration of the *Zeptouniverse* employing rare kaon decays [2]. The measurement of $K^+ \to \pi^+\nu\bar{\nu}$ decay is the main goal of NA62. The importance of this decay is due to its sensitivity to short distances, to the suppression of the Standard Model (SM) contribution and to the good control of the latter. The precision of the SM theoretical prediction relies on the inclusion of next-to-leading order (NLO) QCD corrections to the top quark contributions [3, 4, 5], NNLO QCD corrections to the charm contributions [6, 7, 8], NLO electroweak corrections to both top and charm contributions [9, 10, 11] and extensive calculations of isospin breaking and non-perturbative effects [12, 13]. During the past 20 years we have witnessed a great

advance in the study of the quark transitions as parameterized by the CKM matrix. A single complex phase explains all the CP-violation phenomenology and there is not compelling evidence of physics beyond the SM. Nonetheless, on the quantitative side, the determination of important parameters such as V_{cb}, V_{ub} and γ has not progressed as fast as expected, thus leaving some parametric uncertainty in the theoretical determination of the $K^+ \to \pi^+\nu\bar{\nu}$ branching ratio. Different strategies are proposed to reduce this parametric uncertainty and a state-of-the-art prediction has just been released [14]: $BR(K^+ \to \pi^+\nu\bar{\nu}) = (9.11 \pm 0.72) \times 10^{-11}$. The gap between the theoretical and the experimental [15] precision is wide and will be addressed by NA62.

In 2014 the baseline NA62 detector was deployed and commissioned. The good performance of the SPS, promptly recovering operations after a two year stop, enabled NA62 to accumulate commissioning data and a valuable sample of K^+ decays to verify the expected physics sensitivity.

2 Technical Co-ordination

When the same document was presented in April last year, a long list of *to be completed* tasks was reported. This year one can acknowledge that progress followed the expectations allowing the collaboration to operate an almost complete detector during the commissioning run in autumn 2014 (see Fig.1). Here follows a short summary on the status of each sub-detector:

Figure 1: The cavern shortly before the NA62 run in autumn 2014

- **KTAG** is fully installed and operational;
- **GTK:** the first GigaTracKer detectors were successfully assembled in the summer of last year. The testing and characterization had to be done in a very short time,

practically at the same time of the run start-up. In the second half of the run, three detectors were gradually installed and operated. However, due to time constraints and technical difficulties with the carrier board, the detectors were read out only partially (10%). It was known that the timescale for the completion of the GTK was very tight and, in this context, the essential achievement was to test all GTK sub-systems (detector, cooling, readout, controls, data transfer, etc.) together and in real beam conditions. The data taken are useful for performance studies and to correlate the GTK with the other detectors;

- **CHANTI** is fully installed and operational;
- **LAV:** the LAV detector construction was finished ahead of schedule and the installation plan followed the many dependencies of the general planning. LAV12 was the last Large Angle Veto module installed in August last year. The full system was operational during the run;
- **Straw Tracker:** all four straw chambers were successfully installed and equipped with their services. The SRBs (back-end electronics) development was on the critical path, but were delivered and commissioned just in time for the run;
- **RICH:** the installation and alignment of the 20 RICH mirrors took place as foreseen last summer. A problem occurred during the subsequent installation of the Al beam pipe; the clearance between the beam pipe and the surrounding half-hexagonal mirrors turned out to be very small, causing one of the two central mirrors to lose it's aligned position. The photomultipliers installation, gas filling and readout commissioning were successfully done. The detector has been kept closed and the neon gas will be preserved inside the vessel for reuse during this year's run;
- **LKR / CREAM readout:** the CREAM readout system was installed on time and was fully operational. The LKR/L0 trigger was partially installed (15%) and used for tests during the run;
- **MUV2 and MUV3** were installed well before the run and were fully operational. The CREAM readout was used for the first time on MUV2. The **MUV1** construction in Mainz could not be finished in time and the delivery of this detector to CERN has been delayed to spring 2015;
- **IRC and SAC** were installed and used during the run. The detector read-out was connected to the CHOD electronics based on the standard TDC/TEL62 system;
- **Infrastructure**
  - the cabling of the **vacuum system** was completed in spring 2014 and the system could be successfully commissioned in two steps. The first was in July, when the tank up to tube 28 was evacuated to commission the cryo-pumps and to allow for an intensive leak test of the installation upstream of Straw 4. The second test was made when the final vacuum pumping took place shortly before the beam and passed without any difficulties. The vacuum pressure in the decay region was 3×10^{-6} mbar during the run (see Fig. 2);
  - the two remaining vacuum tanks (tanks number 26 and 28) were received in May last year and their installation followed without any problem;

– the last interface piece for straw chamber 4 was received only in August, but the installation followed without problem;
– the GTK cooling plant was installed in September and commissioned with the detectors during the run. The GTK detectors were operated for precaution at room temperature, but a test run at -25 °C was successfully done in January 2015;
– the PC farm cooling system was successfully commissioned in July 2014.

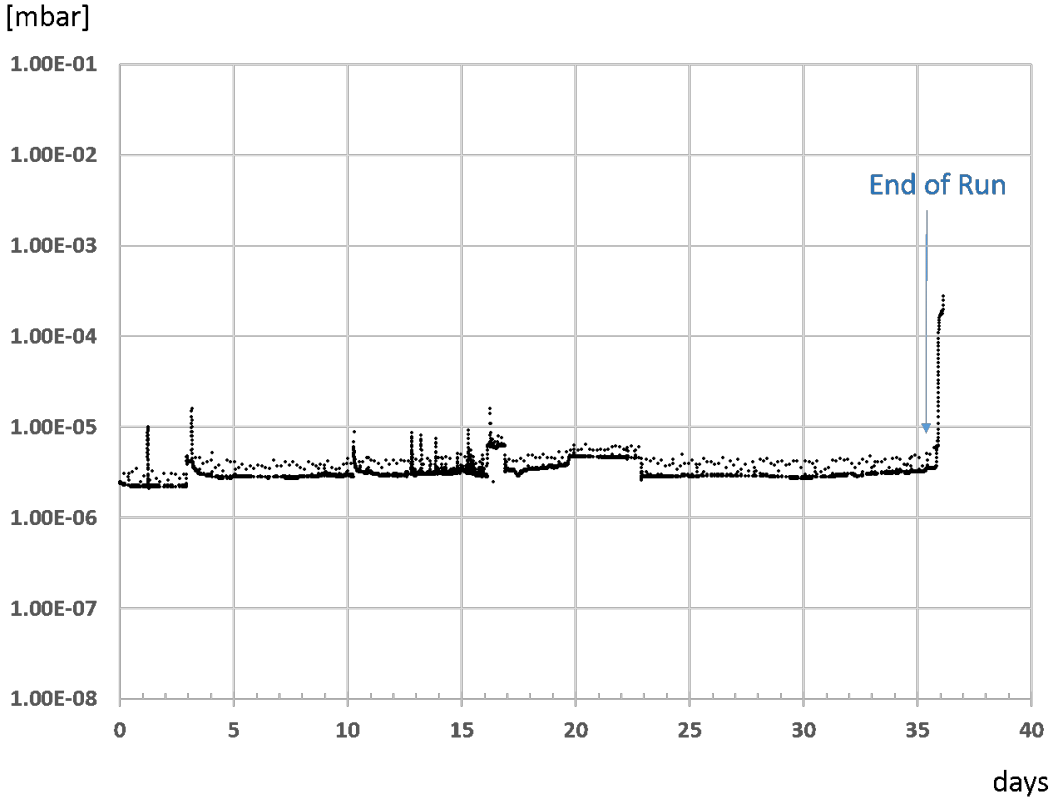

Figure 2: Vacuum pressure in the fiducial region during the run

During the latter half of the 2014 run, we observed several failures of the primary power supplied for the HV crates (CAEN A4531) that are likely to have been caused by single-event effects induced by radiation. In most cases, the faults could be cured by a reset (power cycle), but in a few cases, the MOSFETs on the 12 and 48 V lines were permanently damaged and repair was needed. This type of damage is characteristic of radiation-induced single-event phenomena. We infer the connection between the failures and the radiation from a period when the area suffered from unusually high radiation (see Fig. 3). This run was an anomalous event and probably due to an incorrect magnet current in the P42 line. Such situations will be avoided in the future by enhanced control and monitoring measures which are being implemented. In addition, we are undertaking actions to mitigate potential problems related to higher beam intensity conditions:

- the shielding in front of the CAEN power supplies in TCC8 has been increased. This action is supposed to reduce the effective dose approximately by a factor of 10;

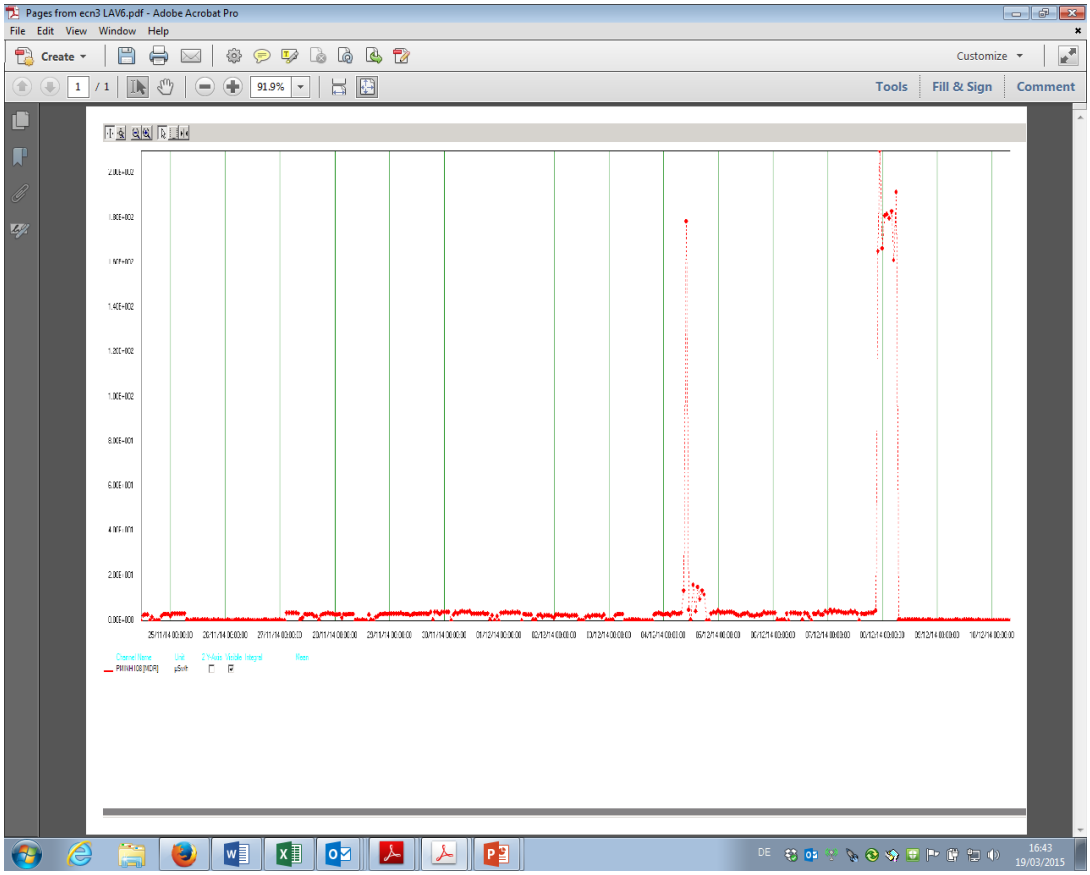

Figure 3: This plot shows the radiation level (unit 1 μSv/h) versus time near LAV6, which illustrates the expected low levels ($<$ 1 μSv/h) for normal beam conditions at 5% intensity. The first peak ($\approx$ 180 μSv/h on December 4^{th}) was caused by beam tuning work; during this time higher radiation was expected and sensitive electronics was switched off. The second peak ($>$ 200 μSv/h on December 8^{th}), however, occurred during normal beam conditions when the electronics were switched on and several failures were observed. The incident was probably caused by a magnet trip in the P42 beam line

- the sensitive equipment (PLC's) in the GTK cooling plant will be moved from TCC8 to ECN3;
- with the help of the EN-STI group and the R2E working group, we are planning to install more sensitive radiation monitoring for the next run. This will enable us to understand better the type and intensity of the radiation in the zones of interest.

3 Beam

The K12 beam line was completely installed and commissioned during the Technical Run in autumn 2012. However, the vacuum tank and the NA62 detectors were only partly installed at the time and the information on beam quality was therefore largely incomplete. Based on the available beam instrumentation, we observed an unexpected asymmetry in the horizontal beam profiles near the KTAG[1] counters and some deficit in the secondary beam intensity per incident proton. At the same time, the current in the first horizontal corrector dipole was unpleasantly large, namely -24 A. This current could have been compensating for a O(1 mm) misalignment of one or more of the front end quadrupoles or larger offsets of the T10 target head or TAX holes, but simulations did not reproduce the observed beam profiles in a satisfactory way. Advantage was taken of the long technical stop to investigate the alignment of all beam elements, in particular the region between (and including) the T10 production target and the dump collimators (XTAX). To check the alignment of the T10 target assembly in a direct way, the fixed dump (TCX) immediately following the target (installed before the start of NA48 and not removed since) and the first quadrupole were taken out. It was discovered that a 60 mm diameter insert with an offset hole of 20 mm diameter hole had come loose and had turned into a wrong position. This insert was removed and the alignment of most of the beam line magnets was further refined.

After detailed beam tuning, the profiles near the KTAG have now become symmetric and the secondary beam flux, and with it the number of K^+ per proton, has become consistent with the nominal one. The horizontal and vertical profiles seen by the FISC counters (Filament SCintillator scanners) adjacent to the KTAG are shown in Fig. 4.

Whilst the flat tails visible on the pair of FISC profiles upstream of the KTAG may be due largely to muons, the enhanced tails on the downstream FISCs are an indication of interactions of the beam in the material of the (N_2 filled) KTAG adopted in 2014. The profile at the downstream end of the beam line, measured with an analog multi-wire proportional chamber, is shown in Fig. 5. All profiles and collimator scans show the expected widths. The current in the first corrector dipole (TRIM-1) now has a very acceptable value of -7 A. In conclusion, the K12 beam is now working as expected.

The P42 beam line, which transports protons not interacting in the T4 target (used to produce the H6 and H8 beam) over 838 m towards the T10 production target of the K12 beam, had not been modified significantly. However, its transmission seems to be significantly lower than in the past, at a level depending on the intensity extracted to the North Area. On the other hand, radiation protection measurements and beam studies show no evidence of any significant beam losses downstream of the TAX dump collimators located 20 m from the T4 target. There are indications that this problem may have been

[1]KTAG denotes here a standard West Area type Cedar counter with modified light readout to cope with the high K^+ rates in the K12 beam line

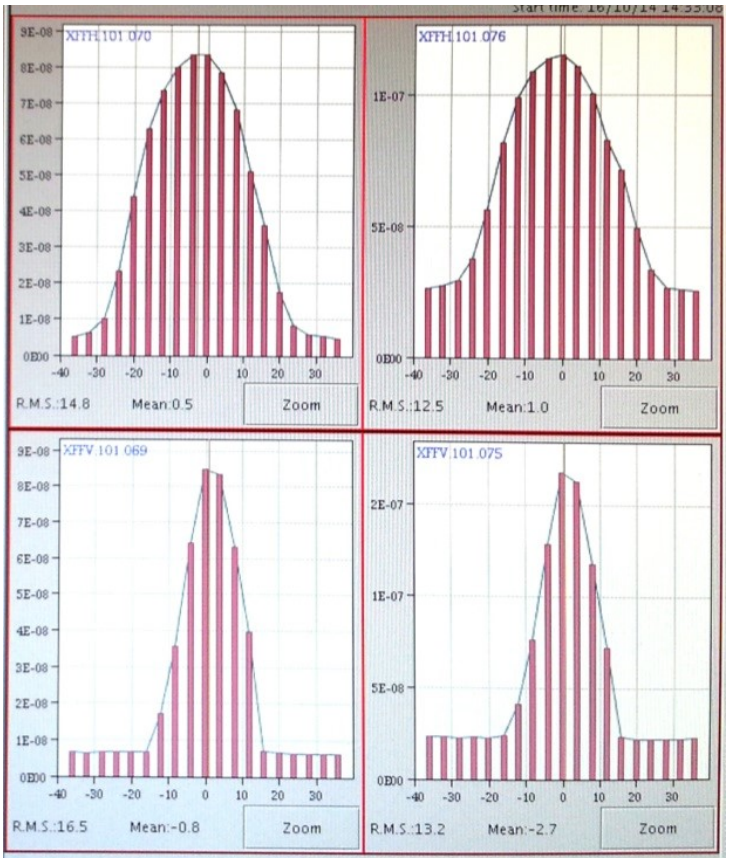

Figure 4: The horizontal (top row) and vertical (bottom row) profiles as observed with two pairs of FISC counters upstream (left) and downstream (right) of the KTAG counter

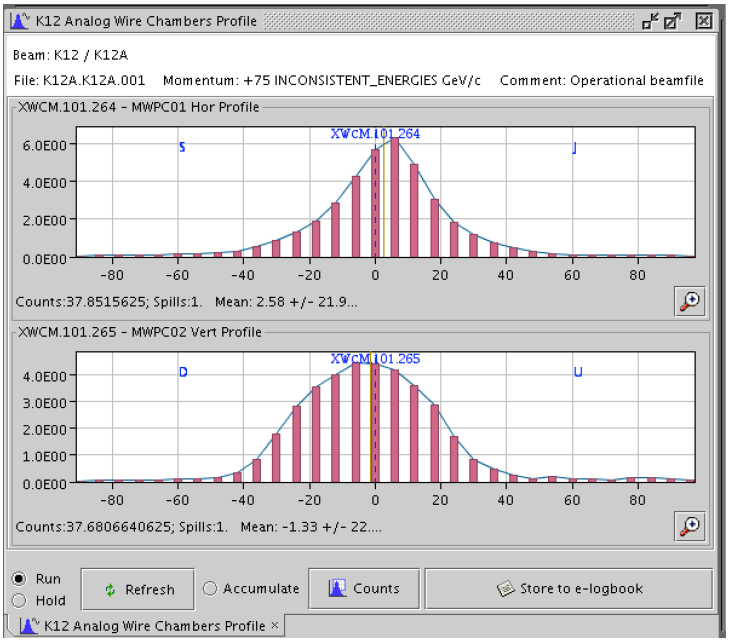

Figure 5: The beam profile (MWPC) at the downstream end of the beam line

there since 2008 (the P42 and K12 beams have hardly operated since then and never at high intensities). The losses are attributed to significant tails on the beam profile at the level of the T4 target, which are clearly seen in the target profiles and confirmed to be real. There are hypotheses about the origin of this problem and mitigation measures will be studied. However, it seems that for the moment sufficient protons can nevertheless be delivered onto the T10 target. Another issue is a significant ripple on the beam intensity with frequencies of 50 Hz and also approximately 100 Hz, already observed just after the North Area extraction. The operations team can reduce these oscillations, but the process takes some time and must be repeated after every change of super-cycle configuration. This affects not only NA62, but all North Area beam lines. Further studies are needed to reduce this problem.

In spite of these SPS related issues, a useful beam of good quality has been delivered to NA62 throughout the run, albeit at reduced intensity, as requested by the experiment. Most of the running was done at 5% of nominal intensity, but during some periods the intensity was increased to 20% and for a short period to 40% of nominal. Several consolidation activities had taken place during the long shutdown. These included a thorough consolidation of the T4 and T10 targets with replacement of all active elements, target boxes and target instrumentation. The fast valve protecting NA62 detectors against a rupture of the exit window of the KTAG has been installed and two magnets were displaced slightly to create a better location for this valve. The vacuum system for the beam line and in particular for the blue decay vacuum tank have been completed and commissioned successfully including the new control system. The kernel of the Cesar beam control system for the North Area has been completely rewritten and many K12-specific applications had to be adapted. Finally, the magnetisation curve (GL versus current) of QNL quadrupoles was re-measured and re-parameterised. This affects 21 quadrupoles in the P42 line and 5 in the K12 beam. The corrections found in the tuning of the focus on T10 were much smaller than in the past[2].

For 2015 the main activity on the infrastructure side concerns the consolidation and upgrade of the ventilation systems in ECN3, TCC8 and the technical gallery GL300. After the run, a problem with the positioning of the last 4-jaw collimator was detected and this will be repaired. The radiation protection monitoring of the air extracted from the cavern will be installed and commissioned. Further refinements of the Cesar beam control system will be made. The beam performance (lateral extent, detector rates and background) is expected to benefit from filling the KTAG with hydrogen gas at a pressure of 3.8 bar (instead of nitrogen at 1.85 bar) and installing three GTK beam trackers of design thickness (≈ 430 μm silicon per station).

4 KTAG

Since March 2014, the KTAG work has concentrated in completing, testing and installing the eight light boxes with the photomultiplier (PMT) assembly, as described in the previous report. The detector was fully assembled by August 2014 with eight completed light boxes, with 48 PMT in each box in a hybrid configuration of 32 R9880 and 16 R7440. The front end and electronics were also completed and tested by September 2014. The Detector Control System (DCS) was improved (see below). The full system was ready

[2]It was cross-checked that this new parameterisation is not responsible for the reduced transmission from the T4 to the T10 target. With the new curve the transmission is as good or slightly better.

for the beam before the autumn data taking.

4.1 Front-end Electronics

The PMT equalization was performed in laboratory in UK using LED and laser light, and the blue index and gain data from Hamamatsu for each PMT; all measurements are referred to a calibrated PMT. Due to the impossibility of reproducing the Cherenkov spectrum in laboratory, the equalization is obtained with a 10% uncertainty. The PMT time resolution and performance were also measured with a laser and they agree with expectations; a small amount of cross-talk has been observed, with negligible impact on data measurements. The revised front-end NINO boards, fully populated with mezzanines, were ready by May 2014; they allow for the full control of the thresholds and HV via the DCS. Besides, more robust connectors give flexibility during installation, which is crucial given the increased number of PMTs, and therefore cables, in each box. The passive 9U splitter boards, designed to connect only 4 PMTs per HPTDC on TEL62 for a maximum of 5 MHz per channel and 30 MHz word rate per HPTDC, were produced, tested and installed by September 2014. Finally, the TEL62 was tested during a radiation exposure at RAL, both with muon and neutron beams. Radiation induced Single Event Effects (SEE) and sustainability to equivalent to the radiation dose expected in NA62 were investigated. Test results showed no permanent damage and verify Single Event Upset (SEU) and Latch-up (SEL) immunity to muons of 90 MeV/c momentum delivering a dose of about 1 Gy. Tests with neutrons in the energy range from 1 MeV to 10 MeV showed no permanent damage up to a dose of about 0.5 Gy, but revealed SEU and SEL candidates in the irradiation process that needed the application of the board recovery procedure. Therefore the possibility of doubling the concrete shielding when running at high beam intensity will be investigated.

4.2 Detector Control System (DCS)

The DCS serves as the Supervisory Control and Data Acquisition (SCADA) for the KTAG slow control, i.e. control of the high voltage, low voltage, thresholds, motor controls and vessel pressure (Fig. 6). The first three are built within the JCOP framework, the latter are operated within the UNICOS framework. Below is a list of the nodes that make up the KTAG DCS project. These run on the production server that runs the DCS projects for NA62 and feed into the central DCS.

For the KTAG pressure vessel (CEDAR) a communication protocol was setup to allow commands to be sent from the DCS to the Gas Control System (GCS). This ensured that control of the valves remained in the GCS domain but allowed pressure set points to be requested and "go to" pressure commands to be sent. This was necessary to allow a pressure scan to be performed. This infrastructure was successfully implemented and tested in summer and autumn 2014. To allow information regarding the status of the system to be stored in the raw data an End Of Burst (EOB) data structure was created within the KTAG DCS and published over DIM. To allow a more integrated system the motor control was brought into DCS (before it was a standalone UNICOS application). The DCS uses a Finite State Machine (FSM) to ensure all the systems are ready for data taking. This has been successfully implemented for the full KTAG logical tree, including all non-standard JCOP components. All these developments were used in the 2014 data taking, with improvements made during the run. The next steps are to improve the user

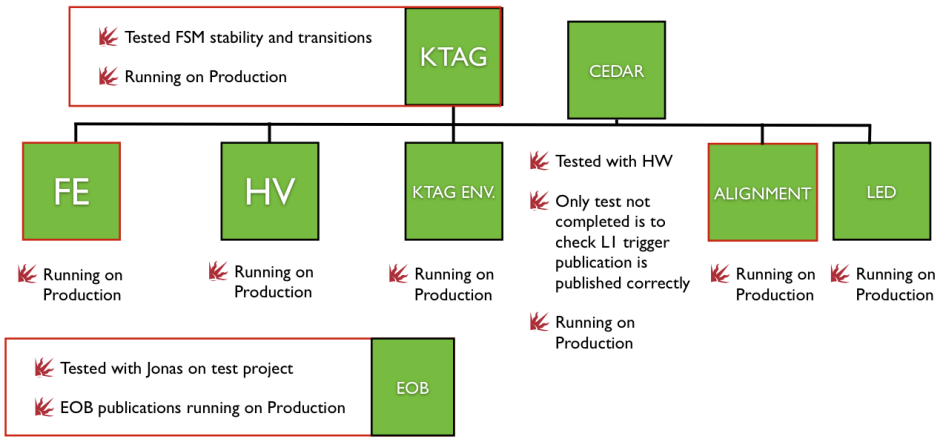

Figure 6: KTAG DCS system

interface and add HV automation to allow voltage scans. The KTAG has further served as a test bed for the development of FSM components used throughout the experiment including CAEN and WIENER units. This continues along with a general widget library to allow homogeneity across the user interface and aid in maintenance.

4.3 2014 Data Taking

During the 2014 data taking, the detector was firstly aligned, and the kaon operating pressure was established. Then the KTAG was synchronised in time channel by channel. After these preliminary operations, kaon candidates are selected as having at least four fired sectors (Fig. 7). A plot of the number of hits per selected candidate (corresponding to at least four sectors) is shown below and has the expected shape. However when compared to identified kaon decays, a reduced kaon tagging efficiency by a few % was observed with respect to Monte-Carlo expectations; the nature of this inefficiency is under investigation, together with a detailed comparison with the 2012 test run performances. Still, the time resolution achieved is 280 ps (RMS) per single PMT, which gives an overall time resolution of 66 ps, therefore exceeding the required performances.

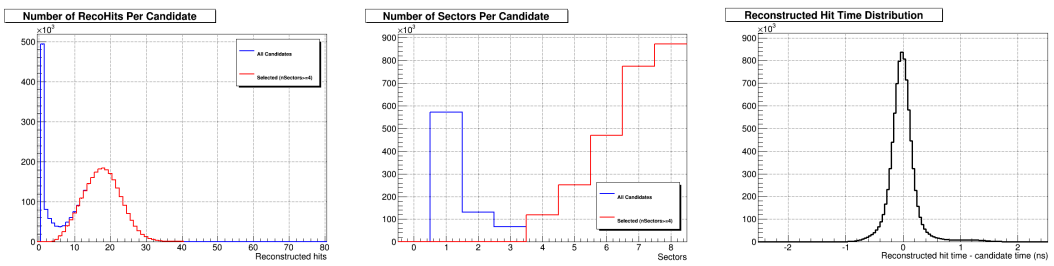

(a) (b) (c)

Figure 7: (a) The distribution of KTAG hits for kaon candidates (number of KTAG sectors larger than 3) is shown in red; (b) Distribution of the number of KTAG sectors; (c) time distribution: KTAG hit - candidate time (ns)

5 GigaTracKer (GTK)

5.1 Introduction

Tremendous progress has been achieved during 2014, granting us the possibility of installing and operate the three stations during the 2014 SPS proton run. However for different reasons, that will be reported and discussed in the present status report, the stations were not fully functional. The list of the achievements includes the followings:

- the ASIC chip, known as TDCpix, has been fully characterized;
- bump-bonding of six sensors with different TDCpix chip thicknesses: 450, 250, and 100 μm, has been achieved;
- first prototypes of the GTK carrier board has been constructed, tested and operated;
- the mechanical integration of the GTK carrier and the Micro-channel cooling system has been accomplished;
- the mechanical integration of the stations in the vessels has been finalized;
- the cooling plant has been constructed, installed and commissioned for a limited set of operating points;
- the DAQ cards have been fully installed and tested;
- run 2014: data were acquired in a "zero-bias mode";
- GTK data are being merged to the NA62 data stream. Preliminary analyses already confirm the good performances of the detector and of the TDCpix.

Due to the inevitable rush connected to the installation we focused the efforts on the characterization and calibration of a single chip per station. The chips, in the three stations, were chosen to be aligned to collect predominantly hits belonging to same beam particle. In the following sections we discuss in more detail the status of the main component parts as achieved for the 2014 run and the expected developments envisaged for the 2015 run.

5.2 ASIC chip characterization

A fully automated TDCpix test bench was produced, which allowed the initials test to be successfully performed in just a few hours. Subsequently the single TDCpix chips were characterized both alone and bonded to a sensor. They were found to exceed the specifications defined by the experiment requirements. So far no errors in the TDCpix design have been identified, which makes the need of a resubmission unlikely. The test bench hardware includes an FPGA processor and a stand-alone cooling unit. The FPGA firmware and the control and data acquisition software were designed in a modular way which allowed their re-use in the NA62 GTK readout system for both the configuration of the chips and the minimum bias data readout mode used during the autumn 2014 beam time. Currently, the single chip assembly is undergoing testing with the high

time precision laser to measure the intrinsic time resolution of the system and permit a comparison with that measured on the demonstrator assembly. The test bench has been expanded to include a probe card and the tests programmes written during the ASIC verification phase prior to submission have been adapted and expanded to include a test suite designed to screen the TDCpix wafers for the next round of bump-bonding. Despite an initial set-back due to an error in the design of the probe card, the design has been re-spun and this work is expected to start in the next few weeks.

5.3 Bump-bonding

The contract signed with IZM foresaw the supply of a pre-series composed of thinned and bump-bonded assemblies made of dummy components and a production-series for the delivery of full-detectors and single-chip assemblies that are thinned and bump-bonded. The purpose of the pre-series was to develop the required expertise for the complex thinning and bump-bonding procedure. In the context of the pre-series, several full-module and single-chip assemblies wereproduced with dummy TDCpix thinned to 100 μm; all assemblies underwent thermal cycles and metrology measurements. The acceptance tests (bow measurements and bump-bonding efficiency measurement via daisy chain electrical tests) were carried out on nine full modules (90% of the production) and completed by mid May 2014. The majority of the modules presented an acceptable bow and very high bump-bonding efficiency ($> 99\%$). The results demonstrated the ability of IZM to proceed with the production of real assemblies. The plan for the production-series, concerted with IZM in May, tried to accommodate for the delay accumulated along this line and in the TDCpix wafer testing, as well as for the very short time available for the complete integration of the GTK. We decide to proceed with two parallel tracks:

- a fast one for the production of two full-module and 6 single-chip assemblies with 450 μm thick readout chip, ready by beginning of July 2014;
- a regular track providing six full-module and 12 single-chip assemblies, half done with 250 μm and half with 100 μm thick TDCpix wafers, for which the delivery was expected by mid September.

All the above assemblies have been done with untested readout chips and arrived in due time. One third of the overall production had to be discarded as broken during the assembly or wire-bonding stage.

The various single-chip assemblies have been used by the team to complete the TDCpix characterization and to study the noise and efficiency maps in the lab test bench.

Three full-module assemblies, the first two from the fast track (450 μm thick) and one (250 μm thick) from the regular track, have been used for the preparation of the three GTK stations. The availability of the first assemblies in July was fundamental for the training of the whole integration and installation procedure of the detector.

Given the lack of time, only few chips per station have been characterized and used during the data taking. The results obtained so far show a very high bump-bonding efficiency.

In January 2015, the details of the next production weredefined with IZM, influenced by the experience acquired in the past months. IZM will deliver nine full-module and nine single-chip assemblies with 100 μm thin readout chips three months after the start of the work. The main changes with respect to the first production will be:

- the provision of tested TDCpix wafers to IZM to allow the selection of working chips (currently foreseen in April);
- the deposition of BCB passivation layers on the sensor guard rings and on the readout chip bands facing the guard rings, to protect the TDCpix from discharges coming from the sensor HV, as we plan to increase the voltage bias of the sensors.

IZM is preparing all necessary masks for the processing of the sensor wafers and TDCpix wafers. A final report on the overall performance of the first batch is in preparation.

5.4 GTK carrier

The GTK carrier is a 10 × multilayer Printed Circuit Board (PCB) which hosts the assembly. It provides all power supplies required by the TDCpix, the very fast control and readout signals to optical components located outside the vacuum vessel and the mechanical interface between the detector assembly and the cooling system. Electrical connections are made by bonding wires between the GTK carrier and the TDCpix, and a similar connection is made for the bias voltage required by the sensor. Each TDCpix requires two different power supplies: 1.3 V digital and 1.3 V analog. In order to minimize the electrical interference, each TDCpix is powered independently. Additionally, 2.5 V, 3.3 V and 5 V are required to power the optical components and other circuits including discriminators and fan-out buffers. This makes a total of 23 power supply connections for each GTK carrier. A picture of the GTK carrier equipped with the pixel detector is shown in Fig. 8.

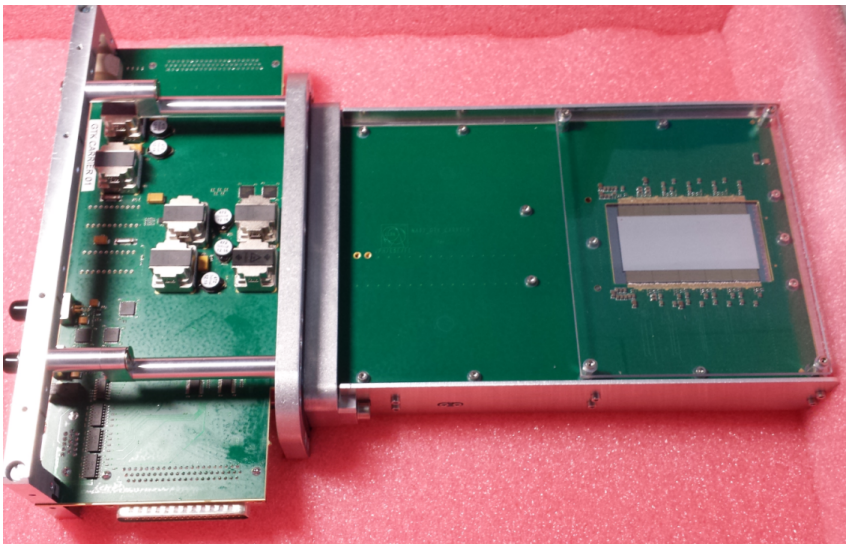

Figure 8: the GTK carrier equipped with the pixel detector

In March 2014 ELTOS was chosen to produce five GTK carriers. After several unsuccessful attempts, the company delivered three GTK carriers at the end of September 2014. These three carriers were equipped with assemblies. Two of them were fully wire bonded and the third one was wire bonded only on TDCpixs #0 and #5 (20%) for the sake of expediency. Despite only being a prototype design, the three GTK carriers were installed in the experimental area and used during the 2014 run. The TDCpix #5 of each GTK carrier were fully operational. The thickness requirement of the countersunk area around the interface to the cooling plate was not properly respected by the company,

so instead of having 515 μm as requested we received GTK carriers that were 1.15 mm thick. This thickness lead to complications with the work of the wire bonding due to a difference of height between the bonding pads and the top layer of the GTK carrier. Nevertheless the bonding lab's team was able to bond the chips by means of a significant manual intervention after the automatic bonding step was finished. When it was understood that ELTOS would struggle to produce the PCBs, we asked another company, SOMACIS, to launch a concurrent production of five GTK carriers. At the beginning of January 2015 we received three GTK carriers that passed all electric tests and one board with two cuts in the signal lines (at a reduced price) which was easily repaired. The four GTK carriers have been populated with the SMD components. At this time one GTK carrier is equipped with the flange and is waiting for the 100 μm or 250 μm thick assembly which will be selected after the probing results.

GTK carrier version 2:

The characterization of the GTK carrier was put on hold during the 2014 run beam period, giving priority to the beam activities. Since this time, a test setup has been established in the laboratory in building 14 replicating as closely as possible the conditions in the experimental cavern. This work is ongoing and although the card operates in many ways as expected, there are several things that can and should be improved for the second version. A list of expected changes follows:

- in order to improve the flatness of the GTK carrier the stack up will be more symmetric, four copper layers will replace the 1 mm inner dielectric layer. The GTK carrier will be produced with 14 layers in total. The new cross section is detailed in Fig. 9;
- the countersink thickness will be fixed at 600 μm and we will ask the company to respect this value;
- an optical reset has been added to the board including a photodiode FTPDA-R155 and associated comparator. The optical reset will trigger the existing power on reset;
- the possibility of changing the mode of each TDCpix using the I2C bus was added;
- 10 $\times$ Conductive Polymer Aluminium capacitors 2V 560 μF have been added close to the TDCpix to improve the drop voltage during the PLL activation;
- 10 $\times$ Electrolytic Aluminium capacitors 10V 4700 μF have been added inside the vacuum side much closer to the TDCpix in order to improve the impedance of the power supply planes;
- the possibility of probing the Mux Analog out signal by using a small connector on each TDCpix was added. A daughter card housing a voltage follower will be connected during the test then removed during the beam operation;
- the level of the serial configuration signals has been modified to properly respect the miniPOD^{TM} requirement for AC coupled signals, whilst maintaining a positive input signal to the ASIC.

The low voltage used by the TDCPix ASICs required some changes to the radiation hard low voltage power supplies provided by CAEN. These changes introduced some

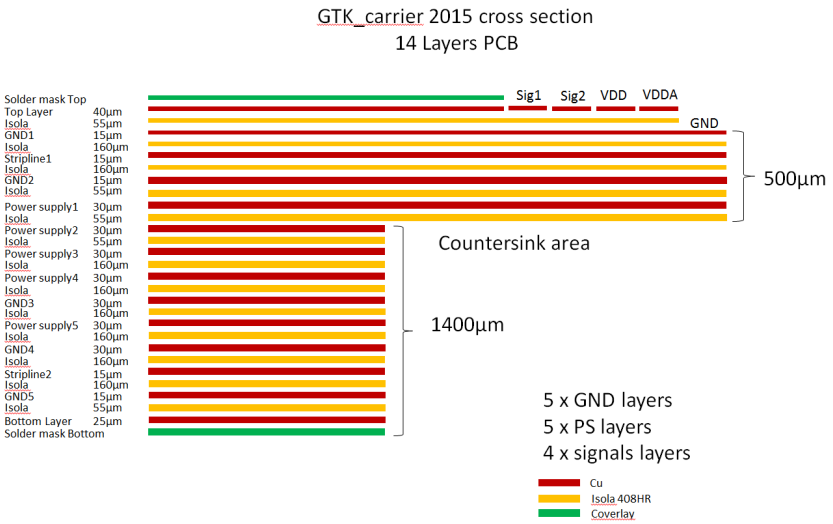

Figure 9: Detail of the new GTK carrier design

issues with the power supply dynamic response and output impedance, contributing to some of the undesirable behaviour seen during the beam period. This issue has been investigated in collaboration with CAEN, and steps towards a solution are being taken.

5.5 Mechanical integration with Micro-channel cooling plates

In 2014, the GTK pioneered the use of silicon microfluidic devices for the thermal management of their pixel detectors and TDCPix readout chips. Two full-scale dummies were fabricated to finalize the design of the various components and to define the assembly procedure. The validation of all the steps of this procedure, from gluing the detector on the cooling plate to inserting of the GTK module in the beam line, was only possible during the second half of the year when all the components were procured at CERN. Three modules were assembled and installed in the experiment according to the schedule described in Section 5.9 (Run 2014). Most of the mechanical components were fabricated at CERN. They were all validated with the first three GTK modules and their production has now been sub-contracted for the 2015 modules and onwards. Some critical points in the fabrication and assembly of the modules have been identified and addressed. The necessary improvements will be implemented in 2015. The status of the different Work Packages (WP) of the mechanics and cooling is summarized hereafter.

- **WP 1 Silicon Micro-channel Cooling Plates**

  Following a prototyping phase on 4 inch wafers at EPFL and a pre-production series on 6 inch wafers at IceMOS, the technology was successfully transferred to 8 inch wafers at CEA Leti. The three GTK modules installed in the beam were equipped with the cooling plates from the first batch supplied by CEA Leti. The first GTK for the 2015 run will also be equipped with a cooling plate from this batch while the others will be equipped with an upgraded version currently under fabrication.

- **WP 2 Microfluid Connectors**

  The vacuum soldering of Kovar connectors to silicon, developed in 2013, was demonstrated on the first cooling plates from CEA Leti. The design of the connectors

was improved and a thorough procedure with a dedicated jig was implemented. It is now a reliable routine operation at CERN performed in collaboration between the PH and EN departments. It guaranteed leak tightness in vacuum of the four connectors of all the plates equipped in 2014 and on the first 2015 plate. The latter has already been characterized in terms of thermo-fluidic operation.

- **WP 3 Capillaries**

  1/16 inch stainless steel capillaries are LASER soldered to the microfluidic connectors and are bent following a pattern that relieves the silicon cooling plate from any mechanical constraint. The 1/16 inch capillaries are brazed two by two on manifolds which route the liquid C_6F_{14} coolant into 1/8 inch capillaries in and out of the vacuum vessel.

- **WP 4 Cooling Plant**

  The cooling plant was installed and commissioned as described in Section 5.7. Additional bypasses were installed on every GTK station along the beam line in order to operate each module independently from the others.

- **WP 5 Thermal Interface**

  A gluing procedure was developed and validated through experimental characterisations of thermo-mechanic dummy detectors in 2013. When applying this procedure to real detectors (see Fig. 10) for the first time in 2014, it had to be adapted due to slight differences between the dummies and the real detectors. The mechanical assembly of the 2014 sensor to the cooling plate was fully functional while the thermal exchange between these two components will be validated at full regime and low temperatures during the 2015 run.

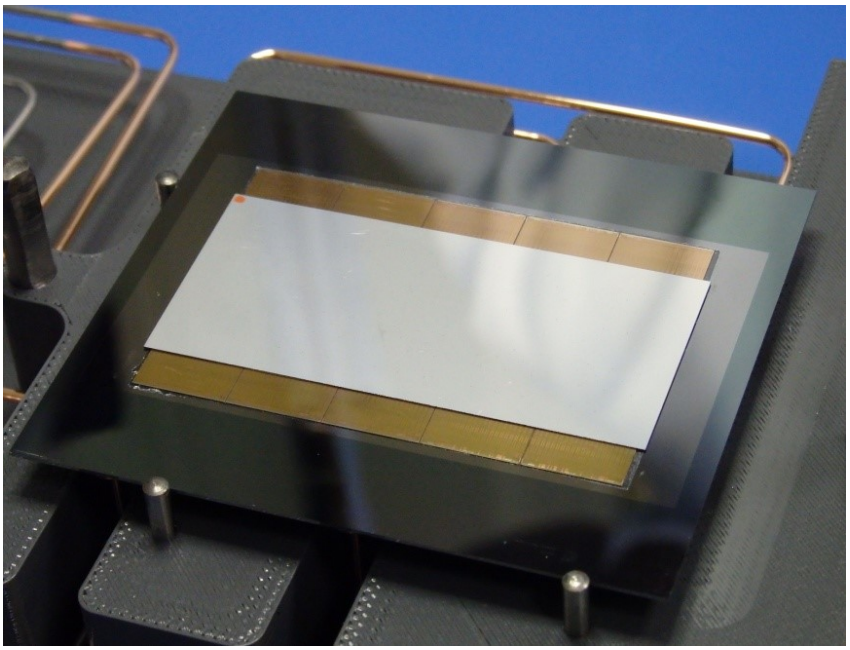

Figure 10: GTK detector bump-bonded to 10 TCPix and glued to the cooling plate

- **WP 6 Assembly to the GTK Carrier and Wire-Bonding**

The three cooling plates with glued detectors and soldered capillaries were integrated into the GTK Carrier PCBs (see Fig. 11 (a)) and TDCPix pads were aligned to the GTK Carrier pads (see Fig. 11 (b)) for the wire-bonding which was performed at the CERN DSF facility. Once the pads were bonded with an automated procedure, all the wires had to be visually inspected and manipulated. This is mainly due to design issues which are currently being addressed in a common effort between PH-DT and PH-ESE following the guidelines from the bonding lab team in order to establish a reliable and efficient production for the modules to come.

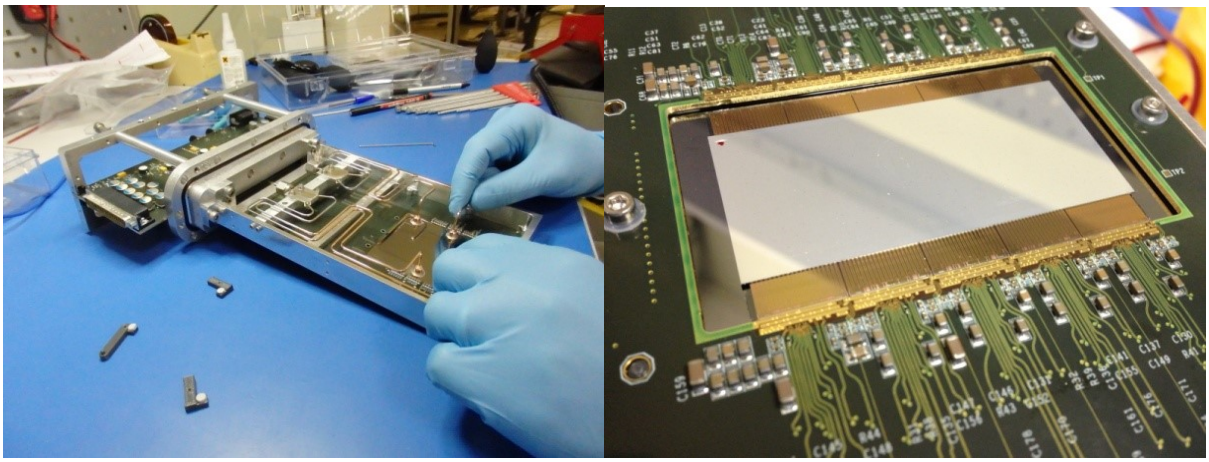

(a) (b)

Figure 11: (a) Installation of the cooling plate with the capillaries onto the GTK carrier and (b) alignment of the pads of the TDCPix to the pads of the GTK carrier for the wire-bonding

5.6 Mechanical Integration with Vessel

The insertion of the GTK modules went smoothly in the three vacuum vessels (see Fig. 12). The flange glued around the GTK Carrier guaranteed leak-tightness during the whole run. The whole gluing procedure and installation protocol was validated and will be repeated for the modules of 2015.

The assembly, installation and operation of the first three GTK modules in 2014 has been a great success. The improvements required to make the whole process more reliable and to operate under nominal conditions are being addressed with the modules under preparation for the 2015 run.

5.7 Cooling Plant

The GTK Cooling Plant has been installed before the end of September 2014 (see Fig. 13). The commissioning has been started right after the installation by circulating the liquid in the external bypass. For the run 2014 the flow was run at ambient temperature and at a pressure of 3.2 bar corresponding to a flow of 7.4 g/s. This was decided not only to avoid thermal shocks on the electronics but mainly because the chips were calibrated at ambient temperature. During the run the operations were rather smooth and satisfactory. Right after the end of the run 2014, commissioning restarted again and a temperature of

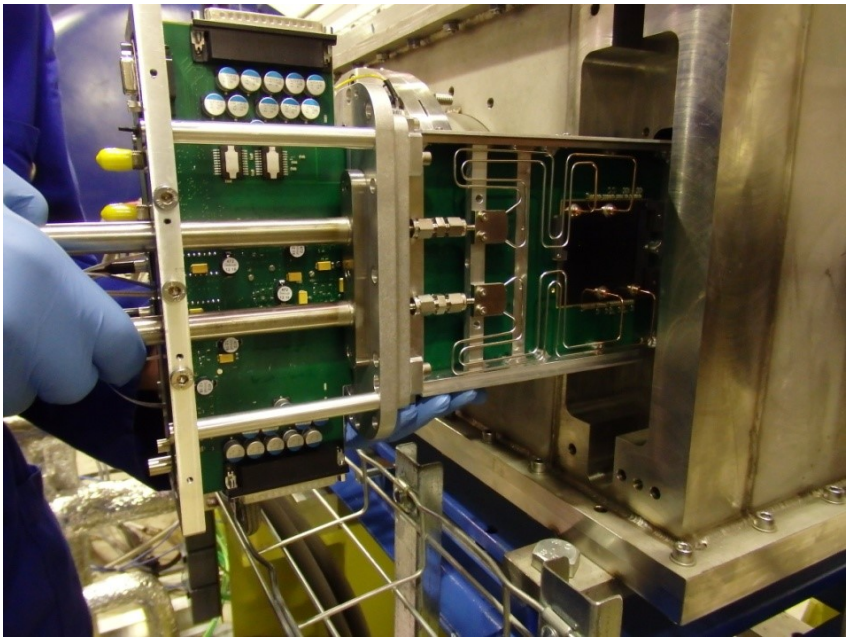

Figure 12: Insertion of the first GTK module in the station 3

-25 °C was successfully probed. The pressure was kept at the same 3.2 bar and the flow, due to the increased viscosity of the liquid, dropped to 3.7 g/s. Range of performances, namely temperature, pressure (which implies flow), and adjustment are under discussion to easy the operation for the coming 2015 run.

5.8 DAQ Status

The off-detector electronics has the main task of receiving the data pushed by the TDCpix ASICs, save it on temporary buffers for the Level-0 trigger latency time, select the GTK data matching the Level-0 trigger request and send packets of events to the sub-detector PCs. These functions are performed by electronic modules in VME format dubbed "GTK-RO". Each TDCpix is served by one GTK-RO module. The latter is actually made of two decked units: the mother board, which is a 6U VME card hosting the main functional blocks, and a daughter card featuring the interface to the TTC system and various timing functions required for the operation of the connected ASIC. In the course of 2014, the GTK-RO motherboards ordered last year have been delivered by the manufacturer. Out of the first trail lot of six pieces delivered only one was rejected due to a malfunctioning FPGA power supply section. The lots delivered afterward all had a malfunctioning power supply section and it was found necessary to rework them to implement workaround solutions. In the end, the GTK-RO motherboards were delivered at CERN in time for the integration with the TDCpix single chip assembly first and the assembled GTK detectors at the time of their installation in the experimental hall for the 2014 run. Simplified versions of the GTK-RO daughter cards have also been prepared to provide the generation and distribution of the timing signals across the GTK-RO cards and to the connected GTK detectors. The readout mode envisioned for the first operation phase of the GTK detectors was the calibration-mode in which all recorded hit timestamps were sent to the subdetectors PC, according to the defined protocol. The firmware of the GTK-RO boards was adapted to support the calibration-mode readout which has allowed to acquire, from the installed GTK stations, a large data set for further

Figure 13: Picture of the Cooling Plant before installation in the pit

alignment and performance analyses. The picture, shown in Fig. 14, was taken during the 2014 run and shows two crates hosting the GTK-RO boards used in the run; one single chip assemblies was also temporarily operated in the PC farm room as a reference system during the system debug phase. During the integration test phase suitable slow control functions were implemented to allow the subdetector PC to control and monitor operating parameters of the GTK-RO boards and of the connected TDCpix chip.

Concerning the hardware development, the activities being carried out in preparation for the 2015 run are:

- verifying and integrating the GTK-RO daughter cards which have been delivered after the 2014 run;
- verifying the performance of the off-detector system when operating in Trigger matched mode (which was not exploited during the 2014 run) taking advantage of the Level-0 Trigger Processor (L0TP) system being developed in Ferrara.

Concerning the software development, the activities foreseen from now until the 2015 run are:

- implementing and benchmarking the "event assembler" code running on the subdetector PC to receive data from the GTK-RO cards (operated in trigger matching mode) and forward it to the PC-farm;
- testing the implementation of the communication protocol, based on DIM, between the subdetector PC and the DCS of NA62.

5.9 Run 2014

The three GTK stations have been installed before the end the 2014 run. All devices inserted into the beam had been extensively tested and calibrated in the laboratory before

Figure 14: GTK DAQ setup

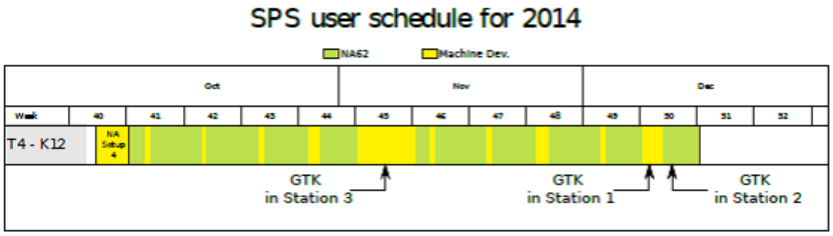

Figure 15: GTK installation with respect to the SPS schedule

hands. Fig. 15 puts in the context of the SPS schedule the date of the three detector installations.

The first station was installed at the most downstream position (GTK3) during the machine development week starting on November 6^{th}. A second detector was then installed in the most upstream position (GTK1) on December 9^{th} and the GTK2 was installed on December 11^{th}. As mentioned in the previous sections, the complexity of the GTK carrier and of the wire bonding resulted in some production defects of the GTK carrier and connections. Hence efforts were focused on getting in all stations the same chip working to reconstruct tracks. This is possible as the beam is collimated to an aperture of 100 μrad at GTK3, particles hit pixels located in the same area on all the stations. We chose to install the two first stations at the upstream and downstream stations as this configuration allows to reconstruct the track direction. For GTK2 the ASIC chips were thinned to 250 μm whilst for the two other detectors ASIC were thinned to 450 μm. As all laboratory tests and calibrations were performed at ambient temperature, we chose to operated the detector in the same conditions at the experiment. The cooling plant flow was set at 3.7 g/s allowing to have a safe pressure drop (approximately 3.2 bar) across

the cooling plate. The three detectors were biased to 200 V for all the period. The three detectors were readout with the final DAQ cards in a the zero-bias mode. Hence despite the rather small acceptance covered by the working chip, significant samples of data have been collected. First results based on this data are presented in the next sub-section.

5.10 GTK Data

All GTK data were collected with a zero-bias DAQ. As a results the GTK data can be merged to the NA62 triggered data to correlate the GTK information to the other detectors on event-by-event basis. The synchronization of the GTK with the rest of the experiment has already been made by looking for coincidence between CHOD and GTK hits as shown in Fig. 16.

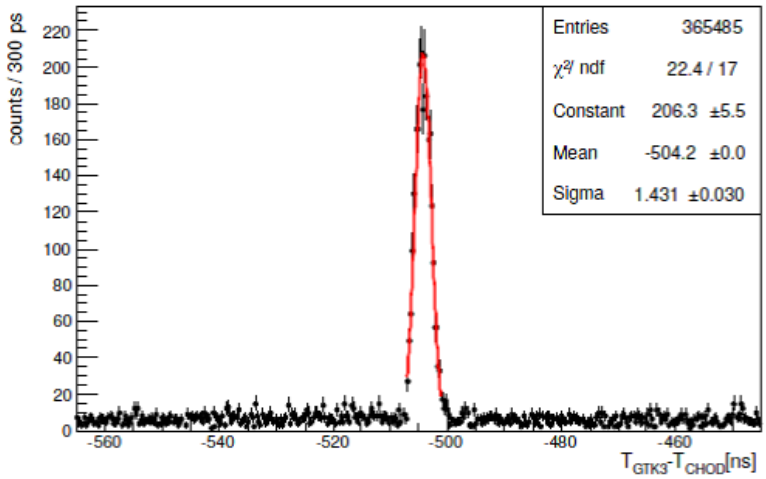

Figure 16: Distribution of the time difference between GTK3 hits and CHOD event time

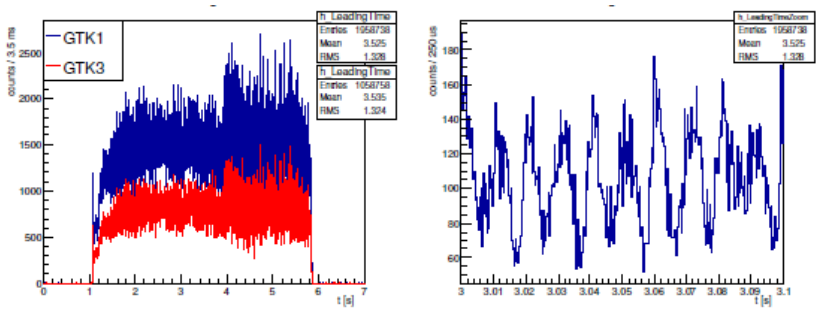

Figure 17: (a) Hit time distribution within a burst for GTK1 and GTK3; (b) zoom of the time scale for the same distribution.

Extracting a time resolution from this plot is premature as no correction to the hit time has been applied and more attention should be paid on selecting a sample of CHOD hits with good time resolution. Zero-bias GTK data provides useful information on the beam structure. Fig. 17 (a) shows the overall time profiles seen by GTK1 and GTK3 for the same burst. The same patterns are found in both profiles.

The hit rate in GTK3 is smaller than in GTK1 as the beam progression is converging and the beam is kicked by 1.2 mrad towards the Saleve by the trim placed magnet 80 cm

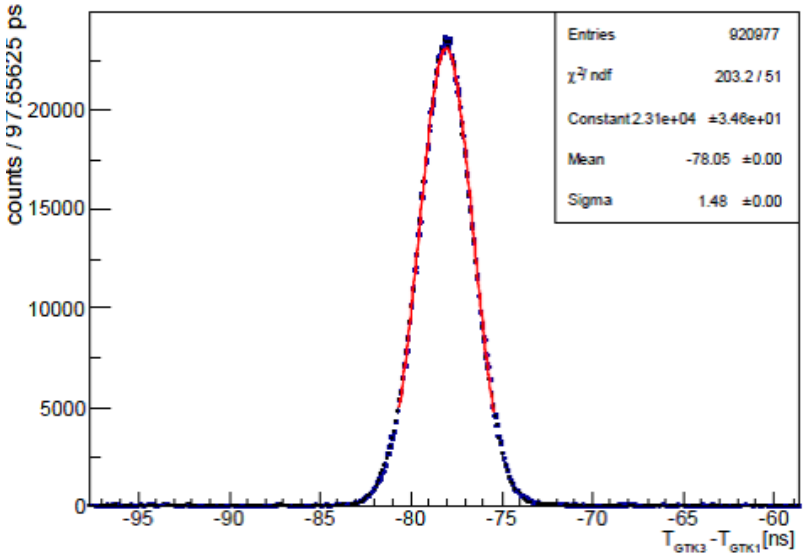

Figure 18: Distribution of the time difference between hits in two stations: GTK3 and GTK1

upstream of GTK3. In Fig. 17 (b) the time scale is zoomed and the known 100 Hz beam structure shows up very clearly.

Data from GTK1 and GTK3 have also been correlated as shown in Fig. 18. The distribution of the time difference can be then used to estimate the time resolution, keeping in mind that at this level are done combining different pixel pairs.

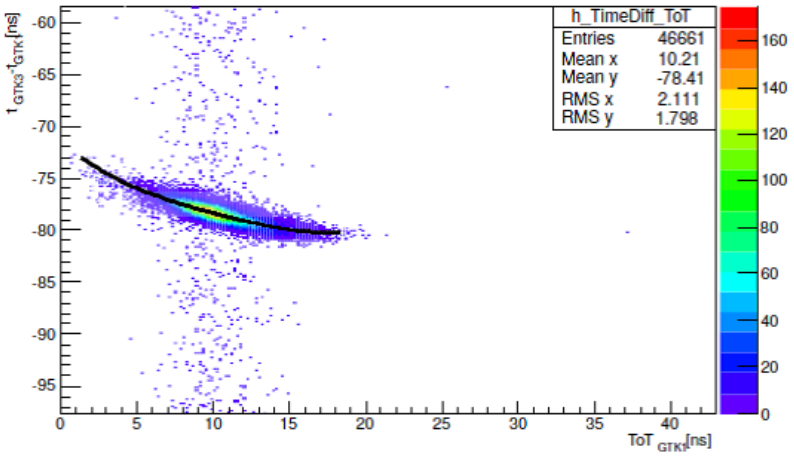

Figure 19: Time difference between GTK1(29,33) and GTK3 vs. ToT of GTK1(29,33)

To extract the most appropriate time one should apply several corrections: a) pixel geometrical position (row and column) with respect to the TDC; b) time-walk as determined from the time-over-threshold measurement; c) finally, a possible correction related to pixel pre-amplifier gain and leading time threshold. Here we report a first attempt to evaluate the time resolution. For this, we selected the pixel for which we have the largest sample of coincidences, namely for GTK1 x=29 y=33. By isolating coincidences with GTK3 pixels and requiring for these pixels a fixed time-over-threshold value, one can consequently neglect the GTK3 time-walk (TW) correction and ascribe to the GTK1 TW all the time deviation. In Fig. 19, we show the distribution of t_{GTK3} - t_{GTK1} as a

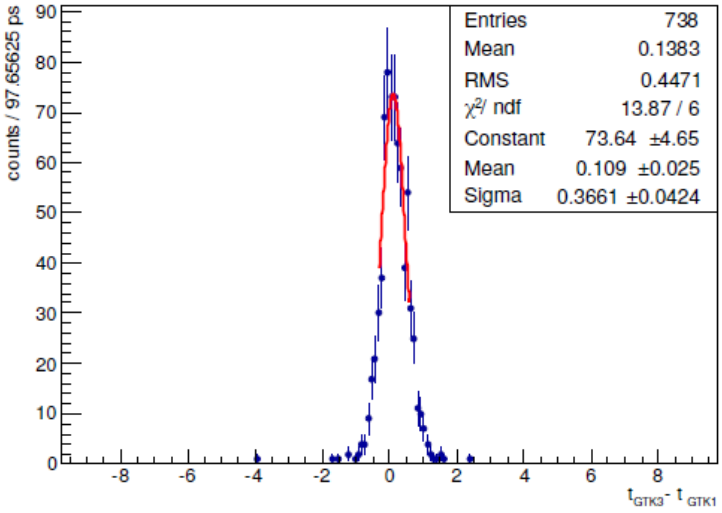

Figure 20: Time difference after GTK1 time-walk correction

function of the ToT of GTK1. A functional correction can then be applied to the GTK1 time and plot again the time difference between hits. To constrain the latency due to the path between a given pixel and the TDC we compared the GTK1(29,33) time to a single GTK3 pixel time. Fig. 20 shows the time distribution for this category of coincidences. The resulting time resolution is estimated to be 260 ± 30 ps which is in agreement with results of the beam test at 200 V bias.

The data collected during the 2014 run demonstrate that the detector is working with timing performances in agreement with the nominal design. These results prove the quality of the detector and also the already good understanding of the data.

6 CHANTI

The CHarged ANTIcounter detector aims at reducing the background induced by inelastic interactions of the beam with the last GTK station, GTK3. It detects the charged particles produced on GTK3 and emitted at relatively high angles with respect to the beam (while the rest of NA62 will be able to detect particles emitted at angles < 49 mrad). It is composed by six 300×300 mm^2 shaped hodoscopes with a 95×65 mm^2 hole in the center to leave room for the beam. Each CHANTI station is made of scintillator bars (of triangular section) read by means of WLS fibers coupled to Hamamatsu Silicon Photomultipliers (SiPM). During year 2014 the efforts on the CHANTI have been concentrated on the finalization of the construction of the detector and of the vacuum vessel hosting both the CHANTI and GTK3, on the test and calibration of the Front End Electronics (FEE) and on the operation of the detector on the beam during the run.

6.1 Construction and tests

The vacuum vessel hosting both GTK3 and the six CHANTI stations is made of two rectangular shaped stainless-steel chambers joint by a 670 mm long tube welded on both sides to the two chambers, so as to form one single 2160 mm long vacuum tight vessel. Both chambers are equipped with flanges and SUB-D 37 feed-throughs to allow for SiPM signals to be carried out towards the FEE boards. The six CHANTI stations have been

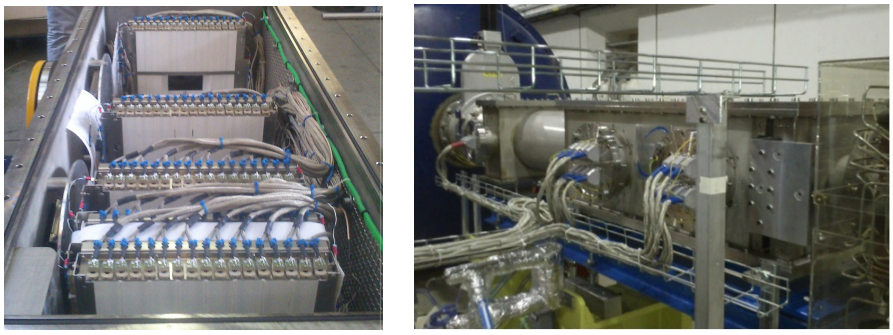

Figure 21: CHANTI assembly in Naples (left), and the final setup at CERN (right)

installed into the vessel and cabled in Naples; then the vessel itself has been delivered to CERN, installed, and carefully aligned to the beam line in July 2014. The GTK3 station has been later integrated into the system during the 2014 run. In Fig. 21 a view of the assembly phase and of the final installation (before GTK3 insertion) is presented.

6.2 Front End Electronics and calibrations

The CHANTI system has a FEE organized on a two level scheme. At first stage the CHANTI-FE boards provide the polarization voltage bias to each SiPM and perform a fast amplification of the input signal ($\times$ 25 amplification factor for 50 Ω impedance). At second stage the LAV-ToT boards, modified to cope with the CHANTI signals dynamic range, provide LVDS Time over Threshold (ToT) signals. These signals are in turn sent to a standard TEL62+TDCB readout system.

A careful calibration procedure for the CHANTI-FE boards has been setup in order to precisely control and readout the value of the voltage bias (whose typical value is around 70 V, and must be kept under control at the 10 mV level) and of the dark current (typical values of few 100 nA). The calibration is obtained by measuring the voltage-current (I-V) curve of a set of high impedance (varying from 500 MΩ to 1GΩ) calibrated input resistors. A final overall scale factor of 0.1% is applied to achieve full agreement on all channels (a 0.07% systematic uncertainty on the resistors' impedance is in fact quoted by the manufacturer). After calibration the CHANTI-FE system was proven to be able, for each channel, to perform absolute voltage/current settings and readout with the same accuracy of a very precise Keythley series 2400 source/meter. In the left plot of Fig. 22 the I-V curve obtained for one typical SiPM channel is compared for the CHANTI-FE (in red) and the Keythley 2400 source-meter (in blue).

Calibration of the thresholds is done at two levels. First of all the DAC and ADC of each channel for each of the LAV-ToT board is calibrated in order to obtain the equivalent value, in mV, for each digital setting of the threshold within the board. Finally, a threshold scan is done for each of the readout SiPMs of the CHANTI system by counting the dark rate at different values of the threshold. Since the SiPM dark rate diminishes by roughly one order of magnitude as the threshold is raised of an amount equivalent to one photoelectron amplitude, a fit of this threshold scan with a proper step function can detemine the amplitude (in mV) of the single photoelectron peak for each channel. This allows to set the thresholds in terms of a quantity directly related to the foundamental process in the scintillator/SiPM (i.e. the number of photoelectrons) rather than in terms of signal amplitude in mV. The amplitude depends indeed on the gain of each SiPM and

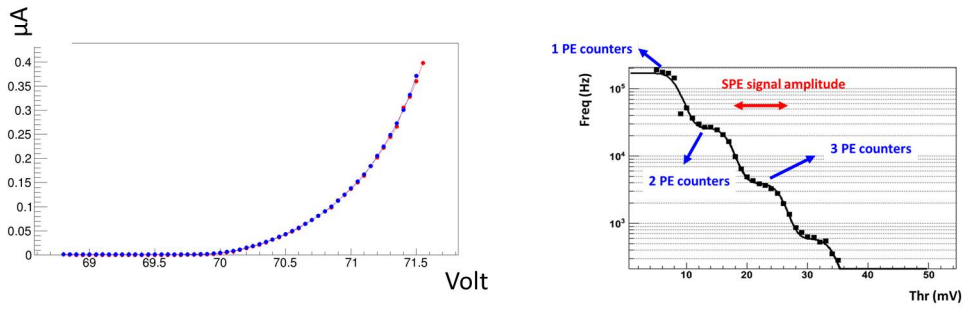

Figure 22: Left: the I-V curve of one SiPM measured with both a calibrated channel of the CHANTI-FE electronics (red) and a Keythley series 2400 source-meter (blue). Right: a typical threshold scan curve. The distance between two consecutive inflection points of the curve is the single photoelectron amplitude. For this particular channel it is found to be about 10 mV.

on the electronics channel amplification gain. A typical threshold scan curve is shown in figure 22 (right) with the fit function superimposed. The same semi-automatic fit procedure is repeatedly applied to all of the channels in order to calibrate the thresholds.

6.3 CHANTI in year 2014 run

The CHANTI was installed and readout since the beginning of the 2014 run. Though the large amount of data collected during the run is still being analyzed, some very preliminary results about its performance have already been obtained. With the limited intensity of the beam, the rate on the detector was expected to be not higher than 100 kHz/channel, rate which has been in fact measured during the data taking on the hottest bars close to the beam hole. The efficiency and spatial resolution have been measured by means of muon halo tracks, which provide a clean sample of straight and penetrating MIPs to work with. Single station efficiency has been measured above 99.9% as expected from laboratory tests performed on the detector prototype using cosmic rays. Regarding spatial resolution, it is worth to note that for the CHANTI the position of a hit in each view is reconstructed as the center of charge of two adjacent bars, i.e. the average of the positions of the two bars weighted by the energy release in each bar. In fact the triangular section of each bar results in a linear (anti corr-)relation between the amount of energy released by a straight MIP crossing the bar and the distance of its interaction from the bar center. This allows the center-of-charge technique to reach a better resolution than the one intrinsic to the pitch of the WLS fibers used in the detector (≈ 16.5 mm $/\sqrt{12}$). Resolution is in fact found to be about 1.8 mm, more than a factor two better. Using the straight muon halo tracks sample, the relative alignment of the six CHANTI stations has been checked: the displacements from nominal positions have been measured to be below 0.5 mm, within the design specifications.

Given the high rate of spurious events crossing the detector (muon halo, pion inelastic interaction and so on), good time resolution is of utmost importance to reduce to a minimum level random vetoes while keeping a high level of efficiency in detecting kaon inelastic interactions. To this aim reaching a few ns single hit resolution is mandatory for the CHANTI. The LAV-ToT boards provide two digital outputs for each channels, corresponding to two different programmable threshold levels. This features allows to

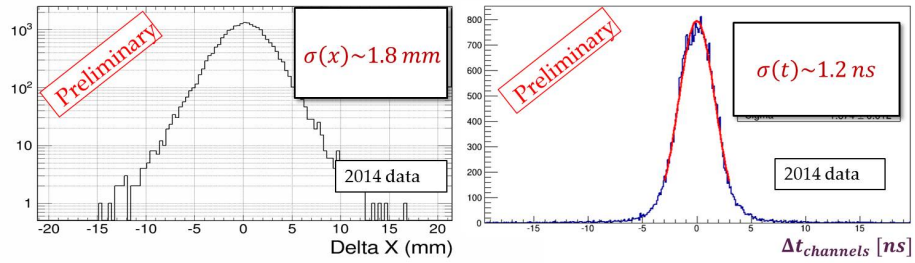

Figure 23: Difference between X position of two hit points on different CHANTI stations for straight MIP selection (left) and difference in time between two bars hit by the same particle after time-walk correction (right). Single hit resolutions quoted are obtained as the RMS of the distributions above divided by $\sqrt{2}$

correct for time-walk effects with a linear extrapolation when both thresholds are crossed by the signal, and to calibrate an average time-walk vs ToT correction, to be used when only the lower thresholds is crossed. Once this correction is taken into account the typical single hit resolution in the CHANTI is found to be about 1.2 ns. Preliminary values for both spatial and time resolution are shown in Fig. 23.

7 Straw Tracker

The Straw tracker consists of four stations, each made of two modules rotated by 45 degrees. Each module consists of two perpendicular views and each view is made of four layers of straws. All four chambers were installed and commissioned in the fall of 2014 and data with all four chambers. The SRBs (Straw Readout Board) were completed and installed and commissioned. The off-detector systems, e.g. the high voltage modules, the low voltage modules and the gas system, were installed and commissioned. The DCS and DSS was commissioned and tested. In particular, the interlocks in case of gas mixer failure or pressure drop in the gas supply lines were tested. Fig. 24 shows the simulated drift time together with data from the run in 2014. The thresholds were set individually on all straws and the hit rates with optimized thresholds are shown in Fig. 25.

One straw out of 7166 showed a leak approximately 1000 times the specification and the gas cell was disconnected. The action for the 2015 run is to block this straw by gluing a plug on each side in situ and operate the other straws in the cell normally.

The straw detector has been fully commissioned and is ready to start data taking in July 2015. An updated version of the firmware of the SRB will allow for trigger matching and the possibility to participate to the level 1 trigger.

8 RICH

The RICH detector is needed to suppress the μ^+ contamination in the π^+ sample by a factor of at least 100 in the 15 to 35 GeV/c momentum range, to measure the pion crossing time with a resolution of about 100 ps and to produce the Level-0 trigger for a charged track. The detector consists of a 17 m long tank, filled with neon gas at atmospheric pressure, with a mosaic of 20 spherical mirrors with 17 m focal length, placed at the downstream end, and about 2000 PMTs placed at the upstream end.

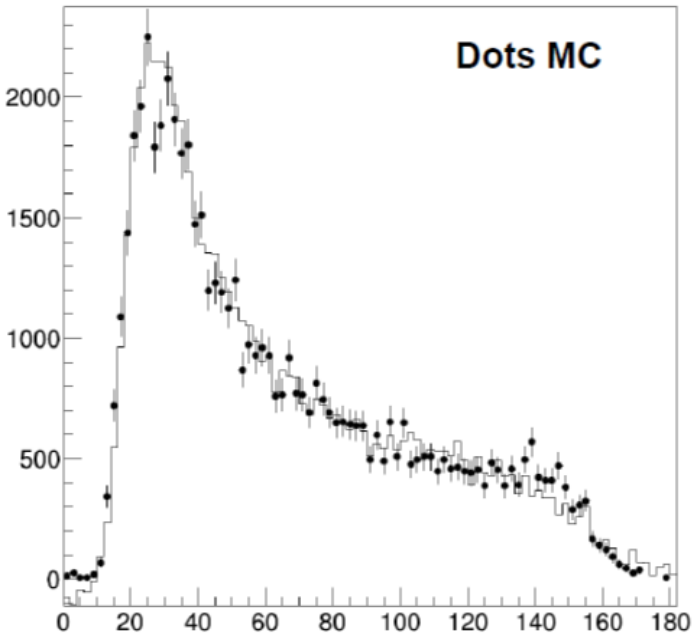

Figure 24: Garfield simulations and data for the drift time of a straw

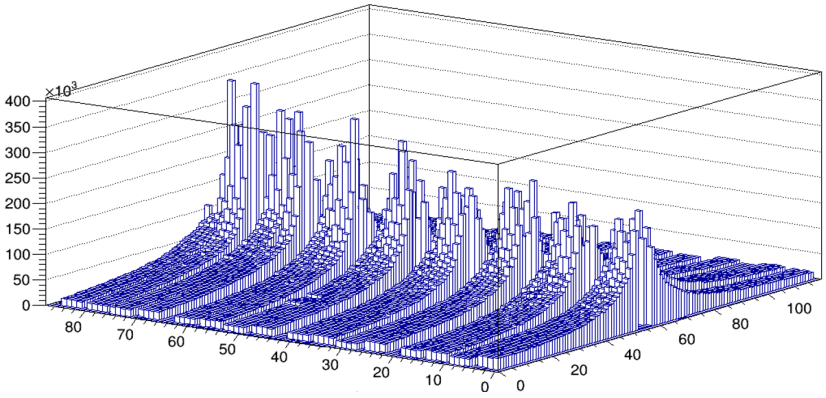

Figure 25: Hit rates in the straws as function of straw position for the four chambers. The 12 cm wide central gap or the beam is clearly visible

8.1 RICH vessel

The RICH vessel is a vacuum proof tank, made of structural steel, subdivided into four drums of decreasing diameter between 3.9 (upstream end) and 3.2 m. A truncated cone shaped part for the connection with the upstream smaller diameter NA62 vacuum tank. The RICH exit window is a refurbished NA48 Al window; the thin entrance window is new. An Al beam pipe will span the length of the RICH to keep the beam particles in vacuum. The RICH vessel installed in the NA62 cavern ca be seen in Fig. 26; the beam pipe seen from the interior of the RICH vessel is also shown.

8.2 Mirrors system

The mirror mosaic is composed by 18 spherical mirrors of hexagonal shape (350 mm side) and 2 of semi-hexagonal shape located close to the beam pipe. An aluminum honeycomb panel has been placed in front of the downstream end-cap of the vessel to support the mirror mosaic. This panel, 50 mm thick and divided into two halves, was carefully

(a) (b)

Figure 26: (a) The RICH vessel installed in the NA62 cavern. (b) The beam pipe seen from inside the RICH vessel; the entrance window and the location of the PMTs disks can clearly be seen

studied to be stiff enough for the 400 kg load of the mirror mosaic and, at the same time, as transparent as possible to photons to be detected from the downstream LKr calorimeter. The support panel was delivered at CERN at the end of April 2014 and installed inside the vessel in May 2014. Each hexagonal mirror has a cylindrical hole, 12 mm wide, in its rear (i.e. not reflecting) surface, close to the geometric center. An aluminum dowel, inserted into the hole and connected to the panel, supports the mirror. Two thin aluminum ribbons, attached at the mirror rear surface at about 250 mm from the hole, keep the mirror in equilibrium and allow its orientation. The semi-hexagonal mirrors have two holes and a single ribbon.

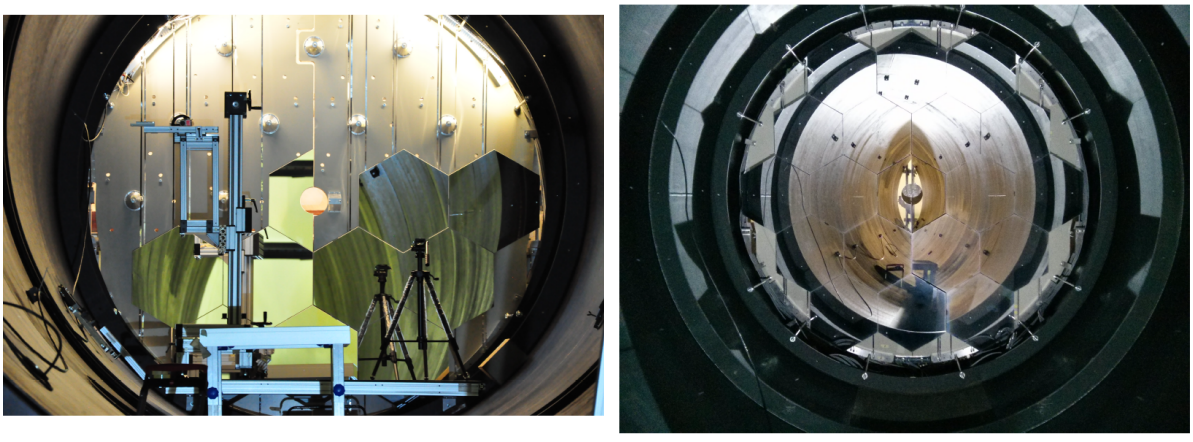

(a) (b)

Figure 27: (a) Some mirrors already hung on the support in the lower part of the mosaic inside the RICH; the loading tool is visible in the picture. (b) The mirror mosaic completed.

The mirror system installation started in May 2014 and was done by technicians from Perugia. The mirror alignment system is based on piezo-motor actuators connected to

the mirrors by thin aluminum ribbons: all the piezo-motors (two for each mirror), with their encoders, were mounted on the support panel in June 2014. The mirrors installation was completed in August 2014. Fig. 27 shows the mirror system installation at different stages. In preparation for Neon filling, the vessel was evacuated, then filled with Nitrogen and evacuated again. Pure Neon gas was finally injected into the vessel at the beginning of October 2014.

8.3 PMT and readout electronics

After installation of the lodging disks, all the PMTs were fully tested with a Laser set-up in a laboratory in Florence before the delivery to CERN in September 2014 and then mounted on the RICH detector. A view of one lodging disk mounted on the RICH vessel can be seen in Fig. 28.

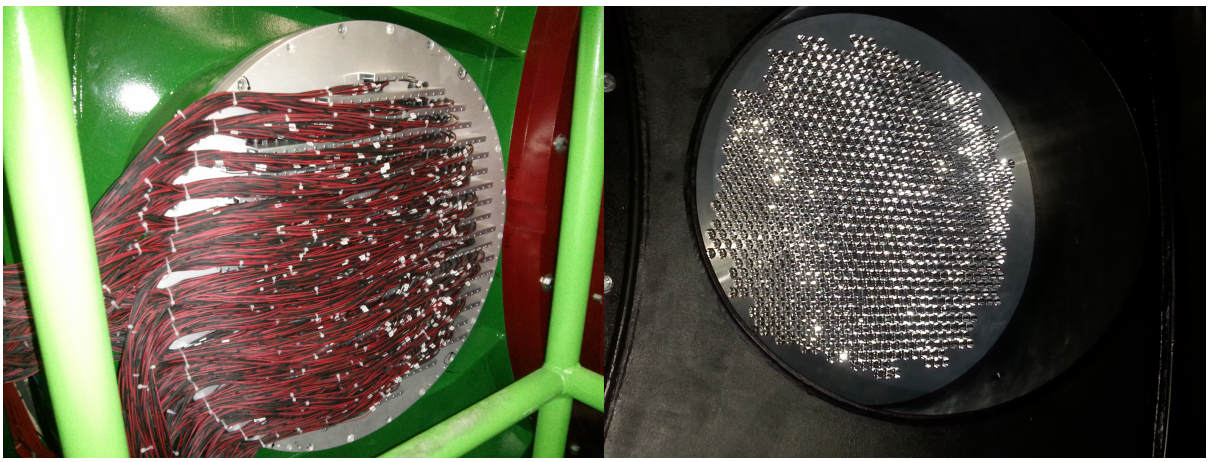

(a) (b)

Figure 28: (a) One of the lodging disks with PMTs mounted on the RICH vessel. (b) View of one of the PMT disks from inside the vessel

The PMT front end (FE) electronics was also custom made and was completed in August 2014. Each FE board, based on the NINO ASIC, has 32 channels and 64 boards are distributed over four crates. The TDAQ system is based on five TEL62 boards (four for the 1952 PMTs, one for the multiplicity readout from the front-end output) of the same type used by other detectors of NA62. PMT cabling (including HV connections, signal connection to FE boards, DAQ connection, DCS connections) was fully completed at the beginning of October 2014. The RICH detector was commissioned at the beginning of the NA62 run in mid October 2014 and some preliminary results are presented here.

8.4 RICH commissioning and preliminary results

A sample of positive pions was selected from $K^+ \to \pi^+\pi^0$ decays, reconstructing the π^0 from LKr information only, using the nominal kaon momentum and direction and requiring the missing mass to be equal to the π^+ mass; in this way the positive pion momentum and direction were reconstructed without requiring any information from the spectrometer. In Fig. 29 the illumination of Cherenkov light produced by positive pions on the RICH PMs is shown for the two PMs lodging disks ("Jura" and "Saleve").

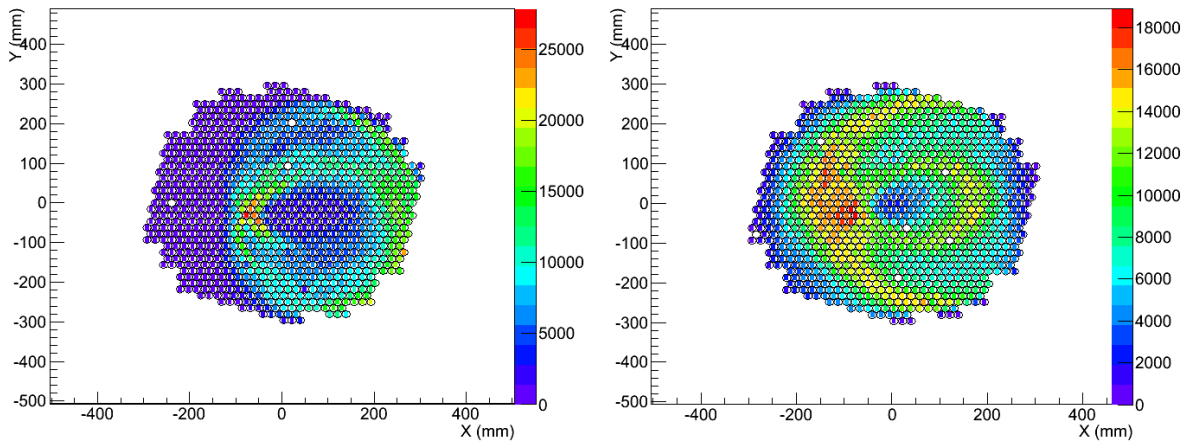

(a) (b)

Figure 29: Illumination of Cherenkov light on the RICH PMs: (a) PMs on the Jura side. (b) PMs on the Saleve side

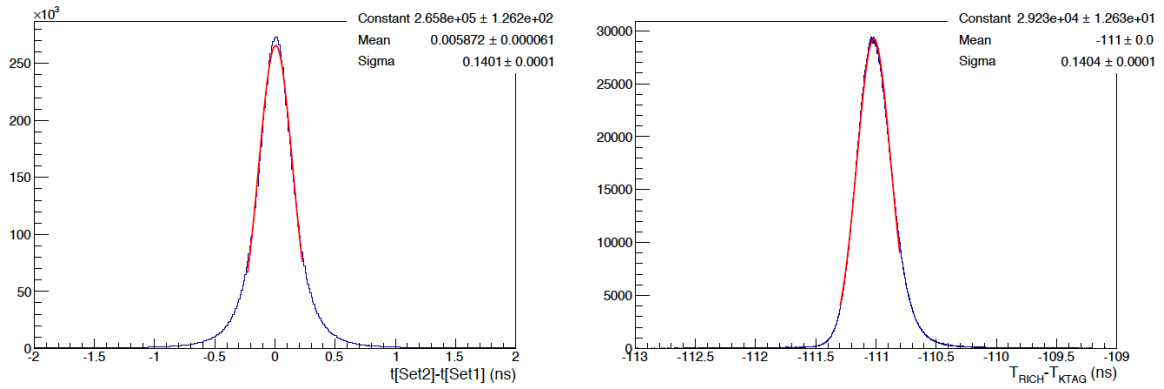

(a) (b)

Figure 30: (a) Difference between the average time of two halves of hits in the same Cherenkov ring: the time resolution of the full ring is one-half of the sigma of the distribution. (b) Difference between the average time of a Cherenkov ring and the KTAG time. A simple gaussian fit is superimposed in both pictures

In Fig. 30 the time resolution of the RICH is shown. In the left picture the hits (one hit is a PMT which fired) in a Cherenkov ring are split into two halves and the difference of the average times is shown. In the right picture the difference between the average time of a Cherenkov ring and the KTAG time is shown. The RICH event time resolution is about 70 ps.

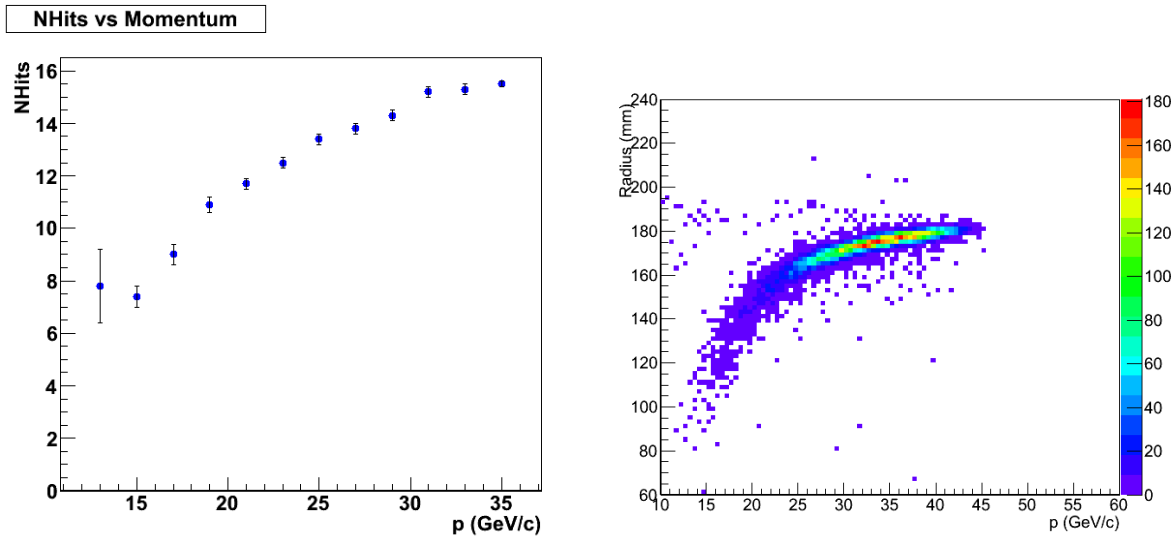

(a) (b)

Figure 31: (a) Number of hits per Cherenkov ring as a function of particle momentum. (b) Cherenkov ring radius vs particle momentum for pions from the $\pi^+\pi^0$ selection without information from the spectrometer

In Fig. 31 the number of hits per Cherenkov ring as a function of pion momentum is shown; the ring radius vs momentum is also shown; the tracks used are pions reconstructed, as described above, without spectrometer information.

The NA62 RICH performed quite well during the 2014 run. The 2015 run will allow us to understand better the performances of the RICH and at the same time this detector will provide the necessary information to achieve the NA62 physics goals.

9 Photon Vetos

9.1 LAV

The principal achievement of the Photon Vetos team in 2014 was the completion of the construction and commissioning of the LAV system, in particular progress was made on:

- construction, testing and installation of the last station, LAV12;
- final cabling and high voltage (HV) testing for all the LAV stations;
- commissioning of the front end and readout electronics for all stations;
- development of the level-zero trigger firmware for the LAV system;
- implementation and optimization of the reconstruction code for the LAV system;

- analysis of 2014 data and measurement of LAV system performance.

The LAV system consists of 12 stations. The diameter of the stations increases with distance from the target, as does the number of blocks in each, from 160 to 256, for a total of about 2500 blocks. Each station consists of four or five rings of blocks, with the blocks staggered azimuthally in successive rings. The total depth of the five-layer station is 27 radiation lengths. This structure guarantees high efficiency, hermeticity, and uniformity of response.

After the installation was completed, all of the LAV channels were tested in two steps. Signals from each channel were first examined manually with an oscilloscope. All 32 input channels on each front end board were then simultaneously pulsed, and data from each board were read out with the full NA62 data-acquisition chain. At the start of data taking in October, inoperative channels were approximately 1% of the total. In all but a handful of cases, the dead channels were caused by problems external to the LAV detectors themselves, often with the HV cable connectors or with the connectors at the interface between front end and TDC boards. In particular, the there were no failures or bad channels on any of the LAV front end boards (including those used to read out the CHANTI, CHOD, IRC/SAC, and MUV3 in 2014).

At the start of the 2014 run, control of the LAV thresholds had not yet been fully implemented in the experiment's DCS system. We used a simple and economical system of Raspberry Pi single-board PCs (one per LAV station) for control of the front end boards via serial link. In the future, this system can be seamlessly interfaced with the NA62 DCS using the DIM protocol.

During the lead-up to the 2014 run, there was significant progress on the implementation of the Level-0 trigger for the LAV system. The NA62 Level-0 trigger receives inputs, or "primitives", from the detectors. These are generated by the FPGAs on the TEL62 boards, which examine buffered data during acquisition, and then forwarded to the central Level-0 Trigger Processor (L0TP), which decides whether to initiate readout. The LAV Level-0 firmware reconstructs physical hits by searching for matching leading edges on the low- and high-threshold channels of each block within a programmable coincidence window, nominally 6 ns; if a coincidence is found, a slewing correction is applied to obtain the hit time. The hits are sorted and hits within a programmable window up to 25 ns in length are merged. The primitive, if generated, contains the timestamp of the acquisition window to read out; the time resolution is 100 ps.

Primitives are continuously generated with a rate of up to 10 MHz, and during the 2014 run were used as a zero-bias monitor of the activity on LAV12. As illustrated in Fig. 32, the spill structure is evident from the LAV12 primitive rate. During the 2014 run, the Level-0 primitives provided the first evidence for the 100 Hz microstructure in the spill seen in the zoom in the right panel in Fig. 32.

During the 2014 run, the Level-0 firmware for the LAV system was used as the basis for the development of the Level-0 firmware for the MUV3 and CHOD, which are also read out with TEL62s. In particular, the CHOD firmware is a reconfigured version of the LAV firmware, and CHOD Level-0 primitive generation was seen to replicate the response of the analogue trigger used during the run.

Much progress has been made on the LAV reconstruction code. Reconstructed hits are assembled by time-ordering the edges for the two thresholds on each block, matching leading and trailing edges, and looking for topologies such as a leading edge followed by a trailing edge on the low threshold only, or, for signals exceeding both thresholds, leading edges on the low and high thresholds, respectively, followed by trailing edges on the high

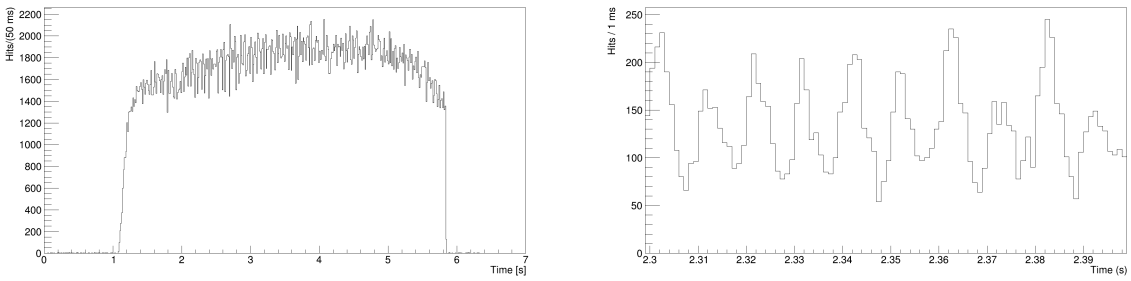

(a) (b)

Figure 32: Continuous monitoring of LAV12 hits from Level-0 trigger primitives, in bins of 0.5 s (a), and zoom in bins of 0.02 s (b), showing evidence of 100 Hz spill structure

and low thresholds, again respectively. Sequences of up to four edges from the same block are thus grouped into a single hit, and the hit time is calculated with channel-by-channel time offsets subtracted and slewing corrected. After hit reconstruction, hits on neighboring blocks are grouped into clusters, starting from a seed hit. Finally, the total charge, energy, time, and position are calculated for each cluster.

9.2 LAV performance studies

We have studied the performance of the LAV system using data collected during the 2014 run. Some preliminary results of these performance studies are presented in the following.

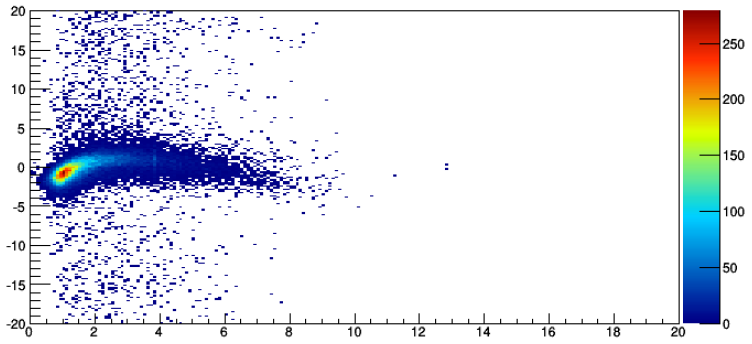

Figure 33: Difference between LAV hit time and event time from KTAG (ns) as a function of signal rise time (ns)

In Fig. 33, the difference between reconstructed hit time and the event time from the KTAG detector is plotted as a function of signal rise time, where the rise time is evaluated from the time between the crossing of the low and high thresholds. As noted above, first-order slewing corrections are performed during hit reconstruction. The effectiveness of these corrections is evident from the figure; the residual dependence observed of the hit time on rise time is parameterized from the distribution shown and applied separately as a final correction.

The distribution of the difference between LAV hit time and event time from the KTAG detector obtained after applying these residual slewing corrections is shown in Fig.34. A time resolution of better than 1 ns is obtained.

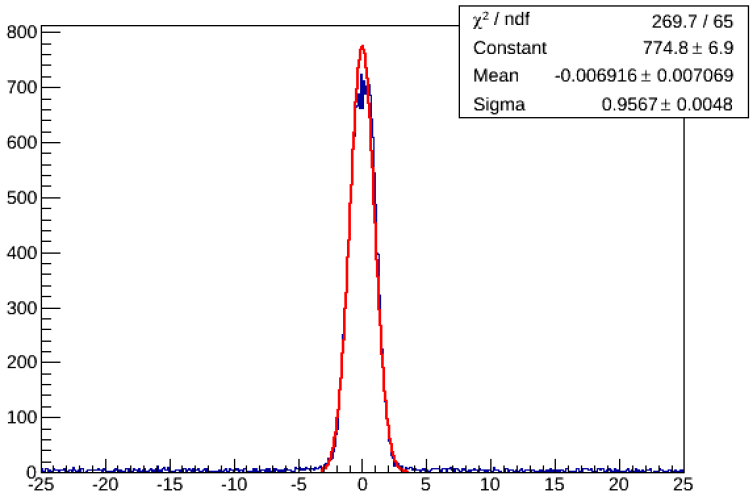

Figure 34: Difference between LAV hit time and event time from KTAG (ns)

Two algorithms have been implemented for the collection of hits into clusters: one for photon clusters, which combines hits on adjacent blocks from an electromagnetic-like shower, and one for minimum-ionizing particles (mips), which combines hits passing through different layers, leaving a track-like signature. Fig. 35 shows the distribution of the difference in azimuth, $\Delta\phi$, between clusters on different stations vs. the number of stations between the most upstream and downstream clusters. Tracks from halo muons crossing many -even all- LAV stations are clearly observed. This suggests an extension of the mip clustering algorithm to provide for the reconstruction of a mip track across LAV stations. This work is currently in progress.

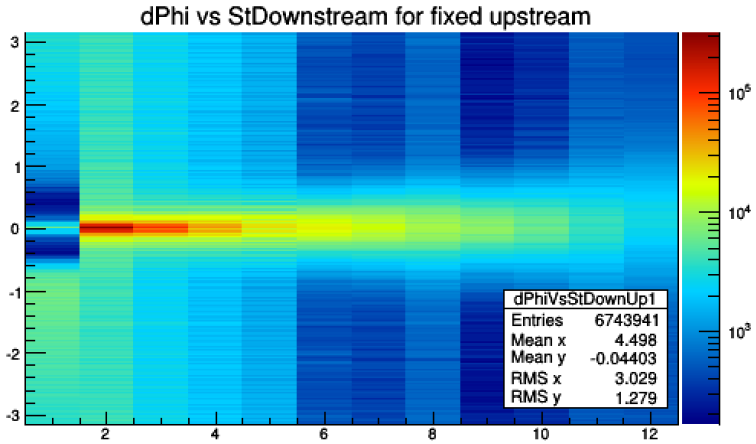

Figure 35: Distribution of difference in azimuth, $\Delta\phi$, between clusters on different stations vs. the number of stations between the most upstream and downstream clusters

By reconstructing hits from the passage of a mip on two appropriately chosen layers of a given station, the mip detection efficiency of the blocks on the remaining layers at

the same azimuthal position can be determined. On two occasions in 2014, data were collected with the TAX collimators closed and the muon sweepers switched off, so that the hadron beam was switched off and the halo muon rates on the detectors increased. During these "muon runs", threshold scans were performed with the LAV detectors and used to study the mip detection efficiency via the method described above. The results are presented in Fig. 36, which summarizes the average efficiency for all 12 LAVs as a function of threshold. The LAVs were operated successfully with thresholds as low as 4.5 mV. For threshold values below about 6 mV, a clear plateau is reached, with all stations reaching 96.5-98% mip efficiency. Recall that a mip passing horizontally through a LAV block leaves a signal of about 12 mV, corresponding to about 80 MeV of deposited energy.

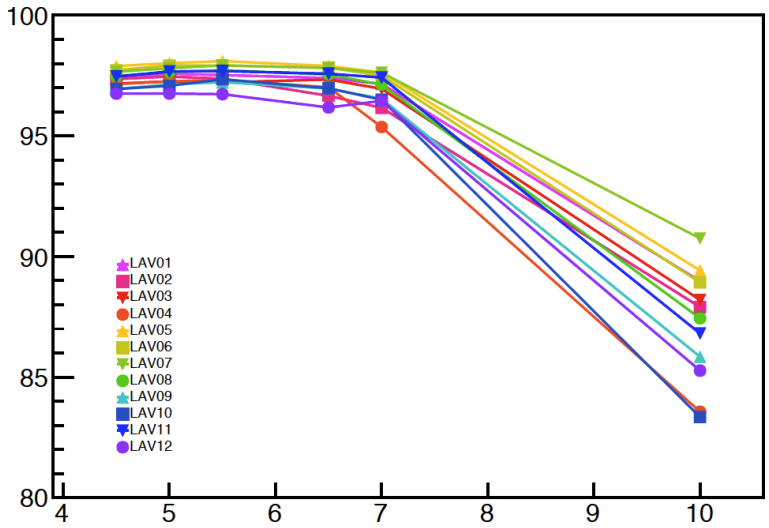

Figure 36: Average mip detection efficiency for different stations as a function of threshold

The photon detection efficiency for the LAV stations can be measured by reconstructing kaon decays for which the kinematics can be completely determined even without detecting a photon in the final state. We have begun to examine the LAV photon detection efficiencies using $K^+ \to \pi^+\pi^0$ events in the 2014 data. These events can be reconstructed on the basis of the candidate π^+ track on the spectrometer and a photon cluster from the π^0 in the LKr calorimeter. Assuming that the K^+ follows the nominal beam trajectory and that the secondary track in the spectrometer is a pion, $K^+ \to \pi^+\pi^0$ events can be cleanly selected by cuts on m^2_{miss} for the $K^+ - \pi^+$ system and $\Sigma E_{miss} - \Sigma P_{miss}$ for the $K^+ - \pi^+ - \gamma$ system. The 4-momentum of the unobserved photon can then be obtained from kinematic closure. This analysis is in progress. To illustrate the potential of the method, Fig. 37 shows the difference in azimuth between the expected position of the photon and the hit found in the LAV. Adding information from the GTK and the final spectrometer, tracking the angular resolution is expected to improve significantly.

Among the activities for the LAV group during 2015, we foresee the following:

- repair of the remaining bad channels and operation of the LAV system at full efficiency during the 2015 run;
- full inclusion of the LAV primitives in the NA62 Level-0 trigger logic;

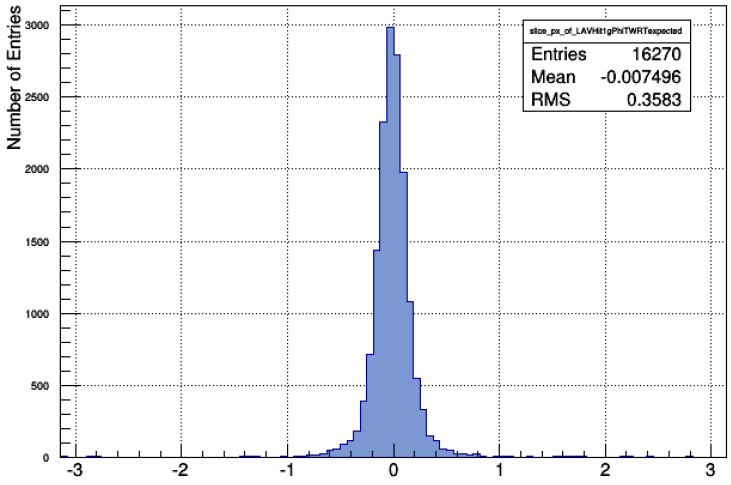

Figure 37: Difference in azimuth (rad) between the expected position of the photon in $K^+ \to \pi^+\pi^0$ events and the hit found in the LAV

- full analysis of the data collected in 2014 to evaluate the performance of the LAV system; optimization of the reconstruction algorithms on the basis of the results obtained;
- integration of the Raspberry Pi based system for threshold control with the NA62 DCS using the DIM protocol;
- production, testing, installation, and commissioning of the LED pulser system to allow in-situ testing and calibration of the LAV lead-glass blocks;
- integration of the LED pulser system into the NA62 DCS.

9.3 SAC and IRC

The SAC and IRC detectors are crucial for vetoing photons emitted at angles of less than 1 mrad. During this year the following tasks were accomplished:

- completion of the IRC design;
- construction, installation, and commissioning of the IRC;
- checks of the 2014 data quality and preliminary evaluation of the SAC and IRC performance.

At the start of 2014, the design of the IRC was completely reviewed at INFN Frascati, and the decision was taken to construct the IRC as a monolithic detector, rather than as two separate detectors modules suspended from the beam tube. All of the components were fixed with respect to the downstream flange of the IRC beam tube, and, in addition, the PMT support flange was glued at fixed position.

Special attention was paid to the certification of the IRC beam tube. Due to its thin walls, the IRC tube is one of the most critical elements of the vacuum system of the experiment. Several different stress tests were performed. The deformation with a

free-floating upstream edge and evacuated tube was found to be less than 10 μm. The evacuated tube was also exposed to an external overpressure 50% higher than nominal for more than 18 hours; the tube did not develop any significant leakage and the vacuum inside was preserved. In addition, a complete finite element calculation indicates that the external buckling pressure is more than 2 bar. After these tests and calculations, the tube was certified for use in IRC construction.

The scintillating plates for the IRC were delivered by the end of June and the assembly of the detector took place in July. Based on the results of a simulation using a purely geometrical model for light collection and signal propagation, a decision was taken to use straight fibers cut in front of the detector, rather than curved and threaded back through the holes. The use of cut fibers decreases the signal width from 25 ns to about 15 ns, which is crucial for double-pulse separation. The complete IRC assembly, as seen in Fig. 38, was shipped from Frascati to CERN at the beginning of August.

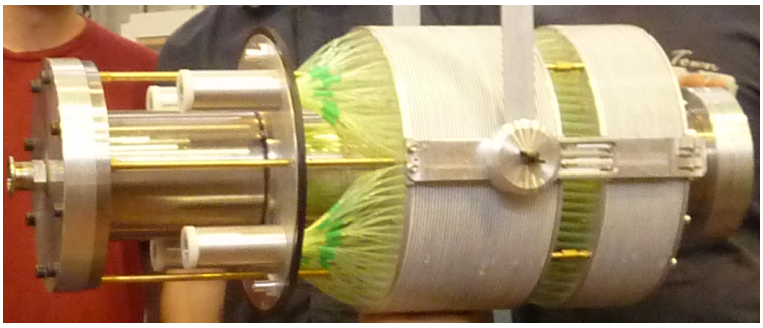

Figure 38: The IRC assembly before shipping it to CERN

Both the SAC and the IRC were installed August and September 2014. They were aligned to a precision of better than 1 mm for each of the reference rod holes, since the IRC is the closest downstream detector to the beam axis, and the 23 mrad rotation angle of the SAC is necessary for high efficiency, since it eliminates the possibility of photons escaping longitudinally via the through holes for the fibers.

Both the SAC and IRC were operated from the beginning of the run. The signals from both detectors were read out with the standard NA62 readout system, based on the LAV front end board developed in Frascati and the TDC-TEL62 chain developed in Pisa. In parallel, a GANDALF-based FADC readout was installed. Although the firmware for interfacing the GANDALF system with the central NA62 data-acquisition system is not yet complete, the FADC system was tested during the run.

A simple online monitor for the SAC and IRC was implemented, based only on the total normalized rate, defined as the total number of hits in each detector normalized to the total number of recorded events for each burst, as shown in Fig. 39. This allowed the monitoring of changes in the trigger definition and beam alignment, in addition to the proper operational status of the detectors.

The response of both detectors to mips was studied with data from the muon runs discussed in the previous section. The SAC and IRC event rates for different thresholds were fit with a cumulative Landau distribution function. The most probable value for the mip signal amplitude was found to be around 4 mV, which is consistent with expectation, and stable in both data sets.

The major tasks planned for 2015 for the SAC and IRC detectors include the following:

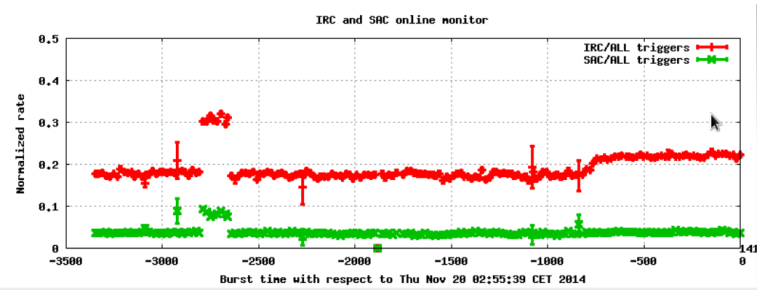

Figure 39: The online monitor for the SAC and IRC

- upgrade of the SAC and IRC readout system;
- development of a method to measure the photon detection efficiency for the SAC and IRC.

10 CHOD

The NA62 experimental apparatus includes a fast scintillator system, called Charged Hodoscope (CHOD), to detect tracks with precise measurements of the arrival time and impact point, to provide a fast signal to drive the trigger and data acquisition (TDAQ) system and to suppress background signals when used in anti-coincidence. The CHOD consists of two planes of 64 vertical and 64 horizontal BC408 plastic scintillator counters, each one read by a Photonis XP2262B PMTs. The counters are assembled into 4 quadrants per plane, installed upstream of the LKr calorimeter. This detector was successfully exploited by the former kaon experiment NA48, with similar purposes. A HV system based on SY403 mainframes, available since NA48, is used to power the CHOD PMTs. A custom control system has been developed for the remote control of this system. New front end and readout electronics are provided to the CHOD in NA62. Four modules of the front end electronics developed for the Large Angle Veto (LAV FEE), consisting of Time over Threshold (ToT) discriminators with double threshold setting availability, and one TEL62 board with two TDCB, have been exploited to process CHOD signals so far. In order to cope with the nominal beam intensity, one TEL62 board, equipped with four TDCB, will be fully devoted to the CHOD in 2015. The channels at high discriminator thresholds will be possibly disabled to keep the TDAQ system working within suitable rate limits. The CHOD is a relevant part of the Level-0 trigger system in NA62 and drives the TDAQ system in presence of charged particles in the decay region. A track signal in the CHOD is given by the coincidence between one vertical and one horizontal counter of adjoining quadrants. The coincidence signal determines the position of tracks impinging the CHOD and allows the track hit time to be corrected for the impact point position on the detector slabs. The firmware for the trigger logic and the time correction for impact point will be implemented in the TEL62 FPGA before the 2015 run, in order to select one or more tracks at the Level-0 trigger level. Given the height of CHOD pulses compared with the discrimination thresholds, slewing effects do not remarkably affect track time precision. The use of ToT discriminators allows a rough time correction due to CHOD small signal slewing. The firmware for slewing correction based on the double threshold feature of the LAV LEE will also be available and possibly applied when both

discriminator thresholds are read. The preliminary CHOD time resolution measured for tracks during the 2014 run has been found to be much better than 0.5 ns after timing corrections.

11 LKr

11.1 Installation of the new readout

In early 2014 CAEN started to deliver the production version of the CREAM modules: by the end of July all the needed modules were delivered. In the same period all the infrastructure was installed (Fig. 40): the 28 VME crates with their VME bridges and the TTC receiver modules, the 28 network switches, all the fibers for clock distribution and network connections and the crate connections to the DCS (Fig. 41). By the end of August 2014 the installation was complete and commissioning had started. As soon as all the cabling related to the CREAM data readout was complete, all the cables for the LKr trigger were installed and properly connected to the CREAM trigger sum outputs.

Figure 40: The complete set of CREAM racks

Particular care was taken to be sure that the environmental conditions in the CREAM room were optimal in terms of temperature and humidity to avoid water condensation

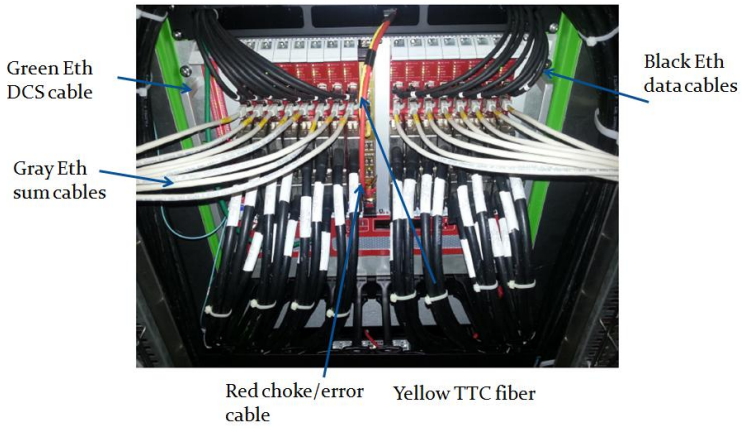

Figure 41: One fully installed CREAM crate

on the heat exchangers, which could lead to water dripping on the electronic modules. A temperature/humidity monitor was installed near the CREAM crate and integrated in the DCS providing SMS alerts in case of trouble. A dehumidifier was running all the time to keep the humidity in the room as low as possible.

On the software side, a set of standalone tools were developed to initialize all the 432 CREAM modules and to analyze data taken with calibration pulses to check the good behaviour of the readout. These last tools are evolving into a standard online tool to monitor continuously out of burst the performances of the readout with calibration data. An additional procedure has been setup to compute the CREAM DAC settings for the baseline definition, starting from a common value, acquiring randomly triggered data, computing the new baseline and the improved DAC setting and iterating until the baseline is within one count from the requested one. This procedure, now semiautomatic, will evolve into an automatic one.

For future improvements, CERN has received from CAEN the complete firmware source code. It is has been successfully compiled at CERN and the output code is being tested in the production system. Among the possible improvements, we intend to introduce a more robust zero suppression mechanism, in order to be less sensitive to the absolute value of the baseline.

A long commissioning phase followed in order to integrate the readout of the CREAM modules within the PC farm software. This activity led on one side to the debugging of the PC farm mechanism to request calorimeter data for any event accepted by the Level-1 software trigger; on the other side it led to debug the CREAM firmware (in tight collaboration with CAEN) to fix problems and improve the functionality. As soon as the run started and the trigger rate increased, a few more adjustments have been done to the PC farm software in order to accept all the events. An intrinsic problem was found inside the network router, where the size of the buffers on the outputs to the PC farm was marginal. This led to a careful tuning of the software in order to smooth the flux of requests to the CREAMs. This eventually led to some changes in the CREAM firmware to have event packing and a more smoother distribution of the output packets.

As soon as the complete system was operational, regular calibration runs were performed. The first goal, before the 2014 run, was to verify all the channels, identify possible problems and verify that the noise contribution of the new electronics was similar to the old one (Fig. 42). Indeed a couple of transceiver boards were found to be faulty and

were replaced. Later calibration runs (Fig. 43) were used to compute new calibration constants (ADC counts to energy). In addition, an updated list of good and bad channels was produced, as well as the new set of digital filter constants for the energy and time measurement. These constants will be used in the offline reprocessing of the 2014 data which will start soon. A software effort was made to port all the calibration software used in NA48 to the NA62 framework.

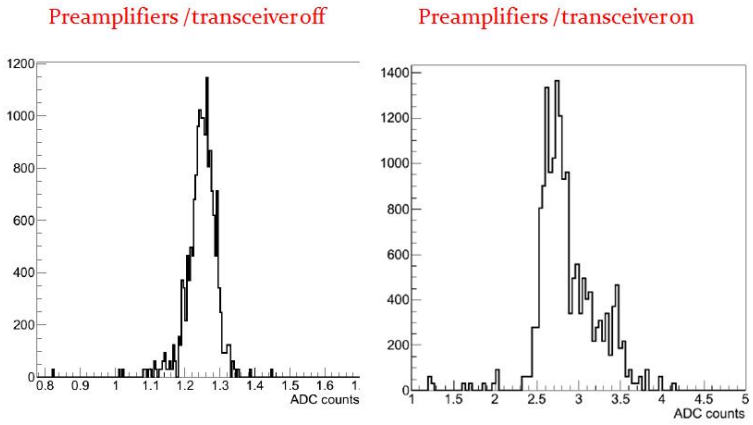

Figure 42: Distribution of the width of the pedestals, without and with front end electronics powered on

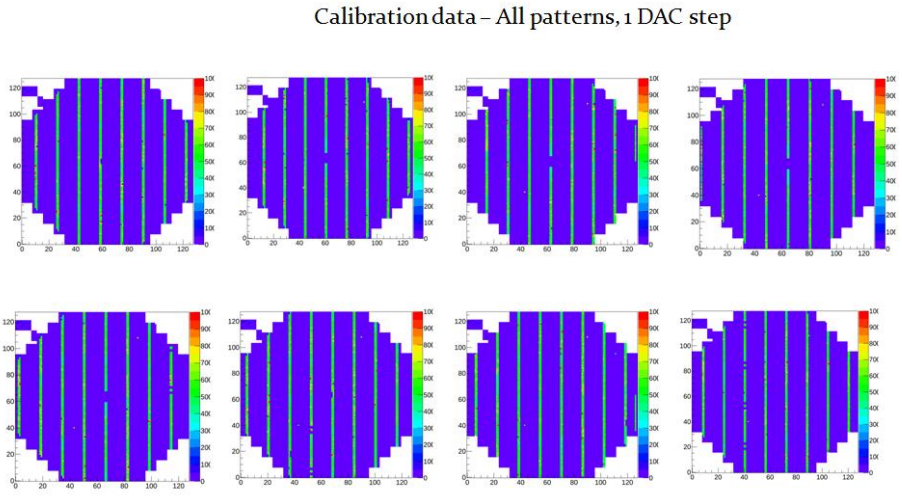

Figure 43: Calibration patterns

12 LKr trigger system

The Level-0 LKr electromagnetic calorimeter trigger (LKrL0), identifies electromagnetic clusters in the calorimeter and prepares a time-ordered list of reconstructed clusters together with the arrival time, position, and energy measurements of each cluster. The trigger algorithm is based on energy deposits in 432 sums of 16 calorimeter cells each

which are available from the CREAM digitizers. The electromagnetic cluster search is executed in two steps with two one-dimensional algorithms (1D + 1D algorithm).

The LKrL0 trigger processor is a three-layer parallel system, composed of 28 front end and eight concentrator boards based on the 9U TEL62 and equipped with custom dedicated mezzanines called TELDES, LKrL0 TX and LKrL0 RX. Each front end board receives data from a vertical slice of up to 32 trigger tiles. The concentrator boards receive trigger data from up to eight front end boards and combine the peaks detected by different front end boards into a single cluster.

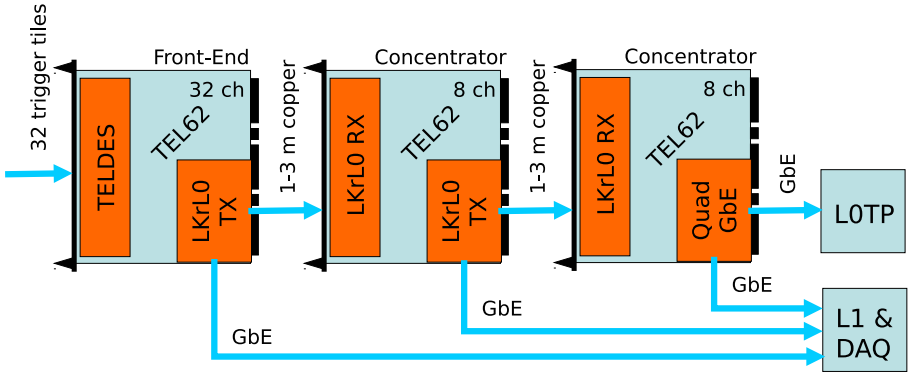

Figure 44: The trigger processor is a three-layer parallel system, composed of 28 front end and eight concentrator boards based on the 9U TEL62 and equipped with custom dedicated mezzanines called TELDES, LKrL0 TX and LKrL0 RX

The TELDES mezzanine receives and deserializes digitized data (16 bit @ 40 MHz over 15 m long ethernet cables) from the CREAM calorimeter digitizer boards.

The LKrL0 TX and LKrL0 RX mezzanines transmit reconstructed clusters (48 bit @ 80 MHz over 2 m long individually shielded twisted pair cables) from the front end to the concentrator cards and between the two layers of concentrator cards. Two 48 bit words (including the payload and error correction code) are needed to transmit energy, position and time of a single cluster allowing transmission of up to 40 MHz of reconstructed clusters from a single 32 tiles calorimeter slice.

12.1 Performance and tests

Six front end and one concentrator boards were installed in the central region of the calorimeter and tested during the 2014 run corresponding to 20% of the whole system. Several tests and checks were performed during the run.

Data transmission from the CREAM to the TELDES was continuously monitored. A DC balance problem in signals transmitted from the CREAM to the LKrL0 trigger was discovered and addressed with a different CREAM trigger sums output encoding. After this firmware correction no data loss was detected in the system.

Long data transfer runs with pseudo random bit streams between the LKrL0 TX (on the front end boards) and the LKrL0 RX (on the concentrator boards) were performed. No error was detected giving a bit error rate better than 10^{-16} (this number can be reduced by increasing the pseudo random bit test run length).

In the final part of the run several tests were performed with the beam. The time alignment of the LKrL0 system was checked respect to the Neutral Hodoscope trigger

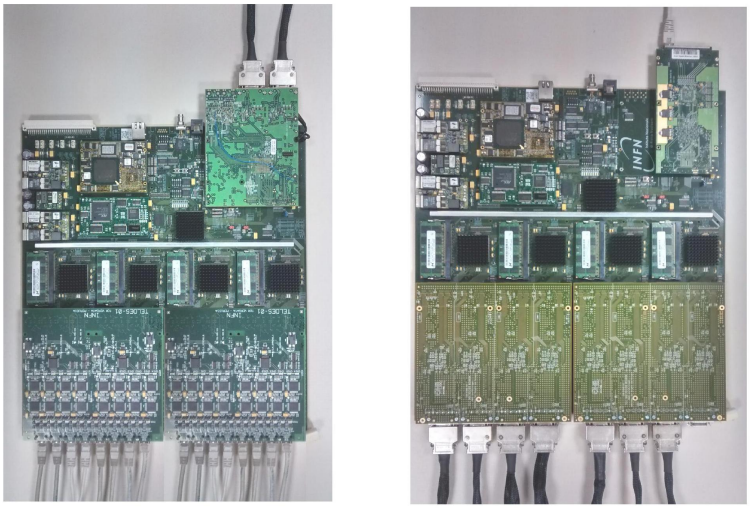

Figure 45: LKrL0 front end board equipped with TELDES and LKRL0TX mezzaniness (on the left) and LKrL0 concentrator board equipped with LKRL0RX and Quad Gigabit Ethernet readout mezzaniness (on the right)

output. The LKrL0 trigger rate per trigger cell was checked and several acquisition were taken triggered by the LKrL0 processor.

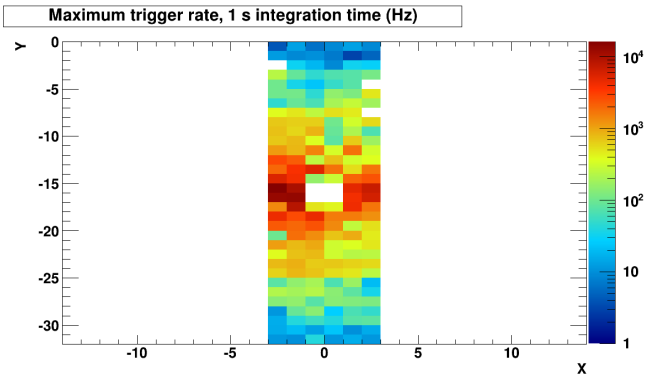

Figure 46: Trigger rate vs trigger tile.

12.2 Production and installation

All the TELDES needed to complete the installation (70 mezzanines including spares) have been produced and are now stocked at CERN. All the LKrL0 TX (50 mezzanines including spares) and LKrL0 RX (24 mezzanines including spares) are currentlty being assembled.

All 432 15 m long halogen-free CAT 6A Ethernet cables needed to transfer digital data from the CREAM to the LKrL0 trigger have been installed. The installation of all the 64 2 m long custom halogen-free cables needed to connect the LKrL0 TX to the

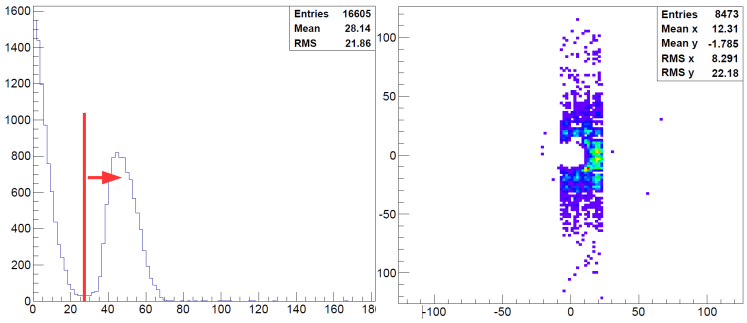

Figure 47: Reconstructed clusters above 30 GeV triggered by the LKrL0 processor.

LKrL0 RX cables is well advanced.

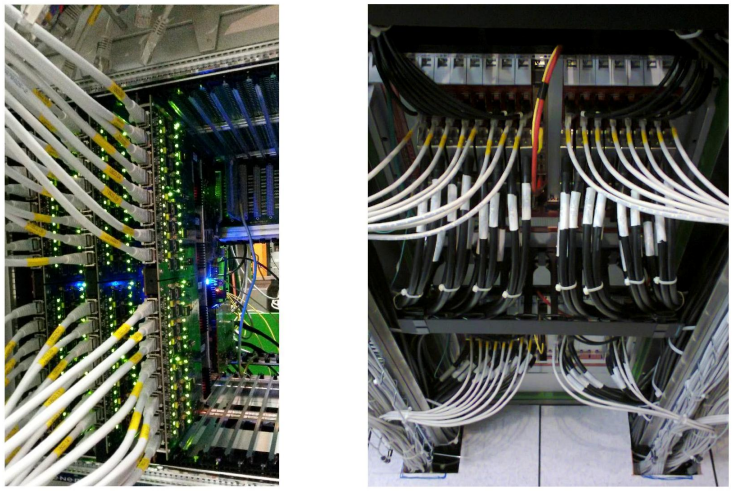

Figure 48: Three LKrL0 front end boards receiving trigger tiles digitized data from the CREAMs during the run (on the left) and trigger tile cables at the output of the CREAM cards (on the right)

Firmware development is ongoing. The core part of the LKrL0 firmware (peak reconstruction) has already been written. System monitoring and concentrator boards firmware is currently being written.

13 Muon Veto System (MUV)

The Muon Veto detector (MUV) is essential to suppress kaon decays with muons in the final state. It consists of three independent modules, following the LKr and called MUV1, MUV2, and MUV3 in the order of their longitudinal position (Fig. 49). While MUV1 and MUV2 are iron scintillator sandwich calorimeters, the MUV3 detector consists of thick scintillator tiles for fast and efficient muon detection on the hardware trigger level.

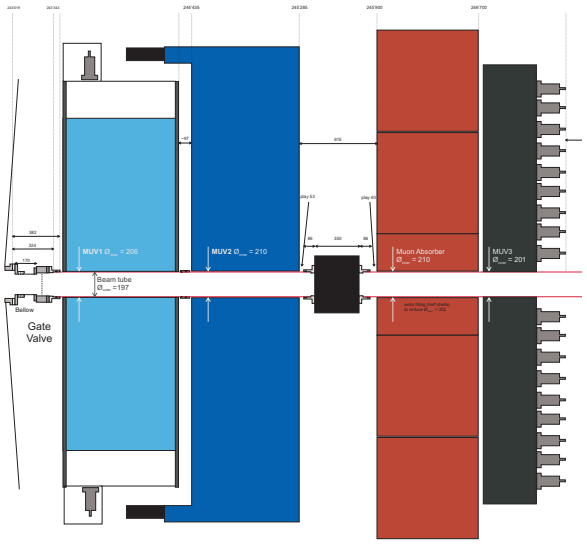

Figure 49: General set-up of the three muon veto detectors MUV1, MUV2, and MUV3

13.1 MUV1 Detector

The MUV1 module is made of 24 iron and 23 scintillating layers with in total almost 1100 scintillating strips. The strips are readout with wavelength-shifting (WLS) fibres on both ends, except for the inner region, where the strips are divided because of high rates and the presence of the beam pipe. The scintillators were produced by the Protvino group with the last batch of 250 strips available in spring 2014.

In Mainz, the scintillators were further processed: each strip was diamond polished, grooves for the WLS fibres were applied, and the fibres were glued in place. Each strip was measured and wrapped into aluminized Mylar foil, and finally installed into the detector.

In addition, an LED calibration system was developed and installed: each scintillating strip was equipped with an UV LED. The LEDs of different scintillating layers can be controlled independently for being able to calibrate single strips.

Due to the late scintillator delivery the MUV1 could not take part in the 2014 run. The construction is now practically finished and the detector will be shipped to CERN in May and installed in the NA62 beamline before the July run.

13.2 MUV2 Detector

The MUV2 detector — the former NA48 hadron calorimeter (HAC) front module — was fully operational in the pilot run in 2014. It was read out with 4 CREAM modules (three for the actual read out and one for a sum of all channels).

The detector performed extremely well in the 2014 run. All channels were fully operating. A full channel-by-channel calibration was done using muons from muon runs (Fig. 50 (left)). After the calibration, the following performances were achieved:

- Attenuation length: the scintillator strips show about 10 % less light output for central hits than for hits close to the sides. This is due to the attenuation within the strips and in agreement with measurements made at NA48 with the same detector module. The scintillators therefore show no deterioration with respect to NA48.

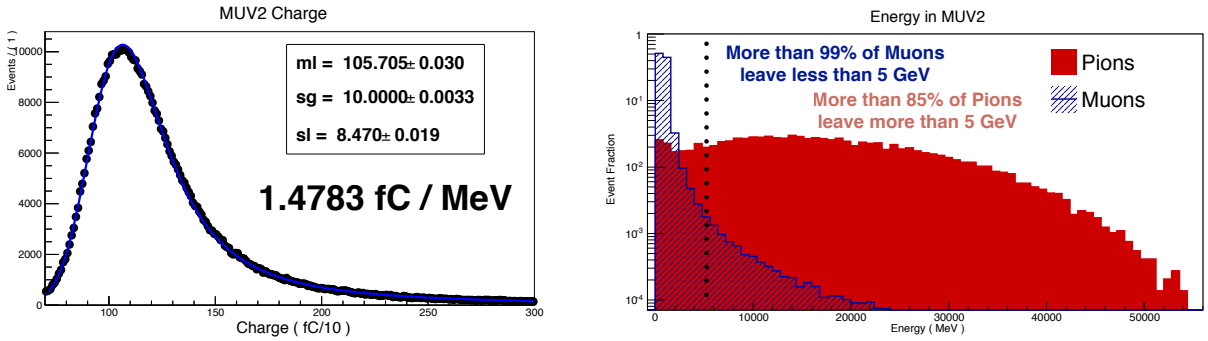

Figure 50: Left: Exemplary charge distribution and calibration of one MUV2 channel. Right: Separation of muons from a muon run and pions from kaon decays in the MUV2 (Particles were requested to deposit less than 5 GeV in the LKr)

- Efficiency: muon tracks from muon runs were extrapolated from the CHOD, the LKr, and the MUV3 to the MUV2 detector. Of all extrapolated tracks within the MUV2 acceptance 99.93 % left a signal in the detector.
- Time resolution: after correcting the PMT times for the hit position, the time resolution of the MUV2 was measured to be about 1.4 ns.
- Pion/muon separation: the MUV2 alone shows already excellent π/μ separation capability. Fig. 50 (right) shows the energies deposited by tagged pions from $K^+ \to \pi^+\pi^0$ decays and by muons from a muon run.

13.3 MUV3 Detector

The fast muon veto detector (MUV3) consists of scintillating tiles of 22×22 cm^2 cross-section and 5 cm thickness, produced at IHEP (Protvino). Each tile is simultaneously read out by two PMTs. As the MUV2 detector, the MUV3 was already running during the technical run 2012.

In the 2014 run, the MUV3 was operated successfully and fully functional, except for the four tiles in the four corners, for which no CFD channels existed. (The CFD electronics should be replaced before the 2015 data taking.) The detector achieved the expected and required time resolution of 0.5 ns (see Fig. 51) and took part in the Level-0 trigger.

14 Trigger and Data Acquisition

The activities within the Trigger and Data Acquisition working group were quite intense in 2014, in view of the commissioning run, while still suffering somewhat from manpower issues. The appointment of an on-site TDAQ commissioning coordinator and dedicated weekly meetings helped in pacing the progress: a detailed and aggressive test schedule was prepared at the beginning of 2014, and although not all systems were fully able to cope with it, it pushed all contributing teams towards coordinated progress. The commissioning run required a sometimes difficult compromise between the needs of the sub-detectors, which required collecting data at low intensity in as stable and uniform

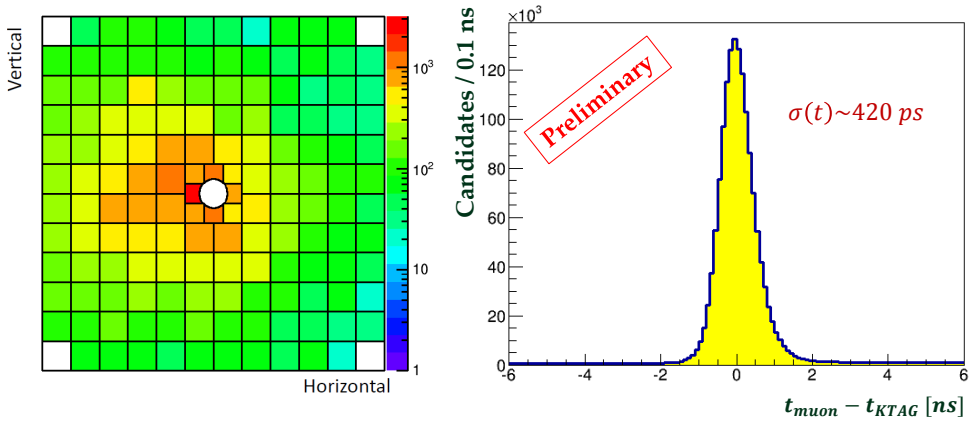

Figure 51: Left: Illumination of the MUV3 plane from muons from $K_{\mu 2}$ decays. Right: Time resolution of the MUV3 detector w.r.t. the KTAG

conditions as possible, in order to gather information on detector performance and calibration, and those of the TDAQ system itself, which required a fast turnaround cycle to identify issues related to actual beam conditions, implement firmware corrections and test them, thus resulting in variable running conditions. Stable data taking was privileged and the time devoted to the debugging and commissioning of the TDAQ system was therefore limited, in particular for what concerns testing in the beam intensity conditions which were known to cause DAQ failures hindering data taking.

14.1 Common infrastructure

The common infrastructure, comprising the clock and trigger transmission system was mostly ready well in advance of the run, and with the exception of backpressure signals, was globally tested showing no problematic issues. The installation of the online farm and its switching fabric was completed during summer 2014, and allowed to achieve the foreseen computing capability. A common and uniform scheme for sub-system run-time initialization and configuration was developed and integrated with the run control, and actively used during the commissioning run for most sub-systems, showing some limitations in the implementation which are now being addressed. The sharing of the run condition information and additional monitoring data to the offline system is being improved as required.

14.2 Common TDC-based TDAQ system

Concerning the common TDC-based TDAQ system used by several sub-detectors, the effort was focused at first on the production, test and delivery of a sufficient number of boards to cover all the requirements for the run; all the TDC and TEL62 boards required were produced and installed on the experiment: this comprises all the boards needed to fully equip the sub-detectors (CEDAR, CHANTI, all LAV stations, NA48 charged and neutral hodoscopes, NA62 charged hodoscope prototype, RICH and its analogue ORs, SAC and IRC), as well as the existing part of the electro-magnetic calorimeter L0 trigger system. As some foreseen manpower for board testing turned out not to be available, and priority considerations required diverting some people from firmware development

to board testing. The yield of boards passing all tests upon delivery was improved significantly from the first pre-production to more than 90% in the final production. The full production of boards is now complete, with a 10% fraction of TDCBs and 20% of TEL62s still requiring testing or repairs: since the beginning of the 2014 run manpower was shifted again on system development and testing, and hardware testing and fixing was put on hold. A laboratory is being set-up in Prevessin to allow quick hardware reparations during forthcoming runs. No significant hardware failures of the boards, neither further crate failures (as experienced during the 2013 runs) were reported during the run. The development of the TEL62 firmware focused on having a version ready suited for low-intensity running, postponing most rate control parts which were assumed not to be highly relevant in 2014. Some limitations were indeed seen in the TEL62 firmware during the run, which were not experienced in lab testing. The first was related to a bug which caused a failure of the system in case a sequence of L0 triggers close in time was received, due to the random occurrence of events even at low intensity. The quick fix was the introduction of a dead time in the L0 Trigger Processor, which allowed bypassing the issue; the bug was later fixed and the fix introduced in the running system at the very end of the run. Another issue was related to a system failure whenever the instantaneous input rate to a section of the TEL62 board exceeded about 75% of the design value, which despite the low-intensity running conditions was seen to occur in several detectors. The required tightly-coupled structure of the NA62 DAQ system, combined with the limited effort put so far on a clean handling of anomalous conditions in the firmware, and a somewhat higher than expected figure for rate fluctuations from the SPS (an acknowledged issue which is being addressed for improvement) led to the loss of data for the final part of each burst in which such conditions were verified. This issue is being addressed along several lines: a new, significantly different, version of the relevant part of the TEL62 firmware (version 3) is being developed, which will allow reaching the design input rate capability of the system (determined by the maximum readout rate of the HPTDC chip) while at the same time improving the capability of absorbing rate fluctuations. This, coupled with a mechanism allowing a "soft" failure - only resulting in a possible (and known) data loss just for the part of the system involved whenever design rate is exceeded for a given period of time - is going to be tested at CERN during scheduled dry runs in spring 2015, while some systems are being implemented to simulate as much as possible beam conditions and thus minimize the amount of beam time required for final commissioning of the system. Some other small issues were experienced during the run, mainly related to the failure in initializing some board at run start, as well as some time offset shifts or loss of efficiency on some individual TDC boards, which are being addressed.

14.3 Online farm

The farm worked satisfactorily, although the fraction of events completely assembled in a burst was not 100%: while part of the dead time fraction could be attributed to individual PC failures, other factors also appeared to play a role, such as frame-dropping in the router and PC memory I/O overloading linked to the running mode with a single event per packet in 2014. Both issues do require further high-data throughput tests. Online monitoring of the above conditions was limited during the run and needs to be improved. No L1 and L2 software trigger filtering could be implemented during the 2014 run, and this issue is now being actively pursued, both at the level of overall software infrastructure

and for what concerns the design of filtering algorithms. Since the overall computing power depends on the efficiency and speed of the algorithms, an assessment will only be possible when these are available, so that a flexible event downscaling capability is being implemented to make sure the system can anyway cope with the existing data throughput. Some urgent manpower issues related to the development of the farm infrastructure are being addressed. During the run, a few failures in network cards required prompt replacement, and some limitations in the cards buffering space was detected and is under investigation. The available network connectivity available for the system was saturated, and investigation on possible expansion is being discussed. The data link to the Meyrin computer centre worked satisfactorily.

14.4 Trigger system

According to priorities, the completion of the digital trigger system lagged somewhat behind the other developments, nevertheless it also saw significant progress. As will be recalled, two alternative L0 trigger processor systems are being developed within NA62: during the first part of 2014, development of the PC-based system was delayed due to the overlap of the development team with GTK activities. The FPGA-based system could instead participate to integration tests and was used as the default system throughout the commissioning run. Still, the development of the PC-based system could later resume, allowing it to be ready during the run, and partially tested during a short period. In order to decouple the experiment data-taking capabilities from the commissioning of the digital trigger system, a temporary approach based on a single simple analogue trigger was adopted and used for most of the stable data-taking periods; this required a simple modification of the FPGA-based L0 Trigger Processor to allow generating triggers in response to an injected pulse and such triggers were then distributed and processed in the normal expected way. The FPGA-based L0 Trigger Processor was used for data taking throughout the entire run and worked satisfactorily, with a few bugs being identified. Different sub-detector teams worked in parallel on the development of the firmware for the generation of digital trigger inputs; for sub-detectors with a number of channels requiring more than one TEL62 board the development focused on single-board primitive generation, since an inter-board communication system was not yet available (it is now):

- LAV: hit matching from LAV station 12;
- MUV3: whole detector hit matching (complete detector on one board);
- RICH: whole detector hit multiplicity, by exploiting an additional TEL62 board receiving as input the analogue OR of all discriminator outputs;
- NA48 CHOD: whole detector hit matching.

Among the above systems, after a first debugging period both the LAV and MUV3 systems were able to continuously generate digital trigger primitives throughout the run: while these were not actually used for trigger generation, they were constantly monitored and stored on dedicated PCs, allowing to verify their behaviour and providing an independent monitoring of instantaneous beam intensity. CHOD and RICH digital trigger inputs were also tested parasitically, but could not be pushed to the same level due to lack of manpower. In a couple of hour test at the end of the run an attempt was made to switch to digital trigger inputs from LAV and MUV3, with inconclusive results later

understood to be due to a firmware error in the L0 Trigger Processor; in a similar short end of run test the PC-based L0 Trigger Processor was also tested, allowing to verify that all trigger input data was correctly processed. The Lkr calorimeter L0 trigger system was partially deployed according to the existing number of interface cards, with the required seven TEL62 boards (six front end and one concentrator) out of the foreseen 38. The production of input interface cards to the CREAM modules was completed, as well as the corresponding cabling. Extensive data transmission tests showed no errors. During the 2014 run LKr L0 trigger primitives were generated on the equipped slice of the detector and checked offline to be consistent with expectations. The possible involvement of the MUV1 and MUV2 detectors in L0 trigger generation is being addressed, in order to provide hadronic energy information which simulation shows to be useful; this could be implemented using a customized version of the LKr calorimeter L0 system. Some limitations of the FPGA-based L0 Trigger System, such as the reduced number of digital trigger primitive inputs and the maximum allowed input rate, which fell somewhat shorter than the maximum design value 13 MHz (which recent simulation work shows to be actually required at full intensity, contrary to earlier estimates), were overcome since the end of the run. As a side development, some tests were performed on a GPU-based trigger for the RICH system, which is being pursued for 2015 by an external team, despite not being strictly required for normal data-taking. Commissioning of the digital trigger is one of the priority items for 2015.

14.5 Conclusions

Summarizing, a very large amount of work was done during the past year, eventually allowing to collect a large amount of data during the run. The TEL62 system, the only one which could be fully integrated within the NA62 infrastructure at L0 trigger level, was extensively used, and some shortcomings were identified which are thought to be related to firmware issues; some fixes could only be tested to a limited extent during the run, and improvements in rate capability and reliability of this system are a priority for 2015, being actively pursued. This experience will be helpful and likely avoid the occurrence of similar issues when fully integrating the remaining systems (straws, GTK). The readout of the calorimeter at L1 trigger level was satisfactory at the rate it was exposed. The digital trigger system was partially deployed and tested parasitically for LAV and MUV3 systems, and is being actively tested now. All the above issues are being strongly pursued to the full capability of the available manpower, with a tight test schedule both at CERN and in outside labs, in order to be ready with a fully working system for the forthcoming run.

15 First Look at the 2014 data

The last two weeks of the 2014 run have been dedicated to take data in stable conditions at about 5% of the nominal intensity. Data were selected by a Level-0 trigger based on fast multiplicity signals from the CHOD, hadronic energy measured in the MUV2 and requiring little or no electromagnetic energy deposited in the scintillating fibre hodoscope embedded in the LKr and in the IRC. Data with a minimum bias Level-0 trigger have also been collected at the end of the run. The analysis of the whole data sample is in progress. During the first week three straw chambers (chamber 1, 2 and 4) were partially read out corresponding to a track geometrical coverage of about 30%. Four

straw chambers have been read out during the second data taking week. The following sections describe a preliminary express analysis of a small fraction of data, as reported in a CERN EP Seminar on March 10 [16]. Those data have been processed using a very early stage of detector reconstructions. In particular:

- **Gigatracker** Not yet used. The kaon nominal momentum and direction have been assumed;
- **Straw Spectrometer** The nominal straw positions have not been corrected offline for geometrical mis-alignments. No single straw calibrations have been introduced. A Garfield simulation of the straw signals provided the relation between the measured drift time and the distance to the wire. A very preliminary fitting code, using a constant magnetic field, has been run to obtain the momentum of the track candidates;
- **RICH** Offline corrections for geometrical mis-alignments of the mirrors were not yet considered.

15.1 Single Track Analysis

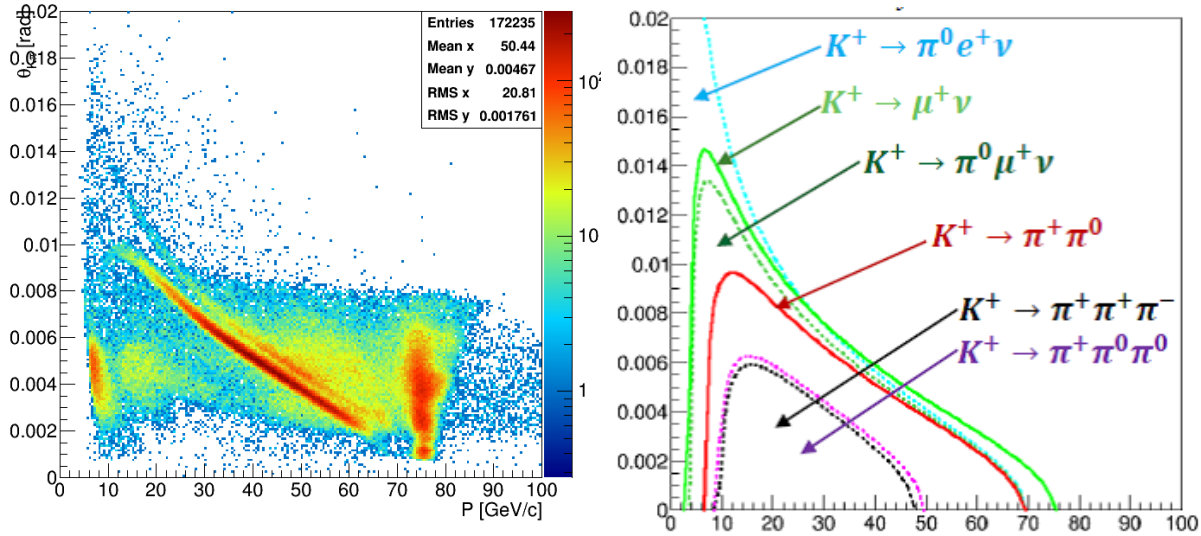

(a) (b)

Figure 52: (a) Angle between the reconstructed track and the nominal kaon direction as a function of particle momentum [GeV/c] in data and (b) as expected from pure kinematics

This analysis has been performed on a percent fraction of data taken with three straw chambers. Events have been selected requiring exactly one track reconstructed in the straw spectrometer within ± 40 ns from the CHOD time. The average trailing time of the straw signals forming a track defines the time of the track with a resolution of about 6 ns. Fig. 52 (a) shows the angle between the track and the kaon direction as a function of the particle momentum measured by the straw spectrometer. For comparison, Fig. 52 (b) illustrates the theoretical curves in the angle-momentum plane expected from

kaon decays. Data cluster along the $K^+ \to \pi^+\pi^0$ and $K^+ \to \mu^+\nu$ bands and in the $K^+ \to \pi^+\pi^0\pi^0$ region.

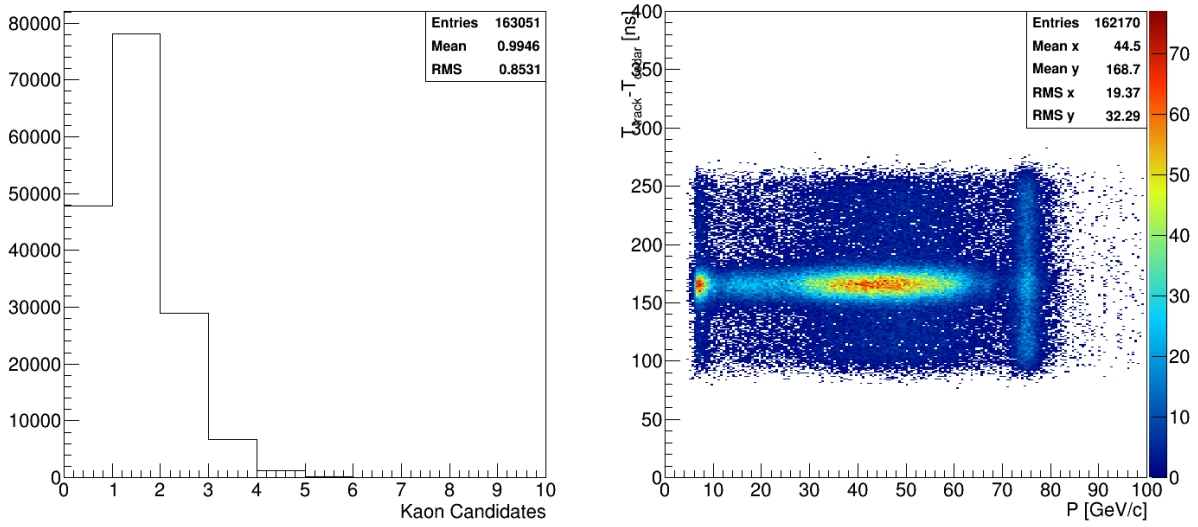

(a) (b)

Figure 53: (a) Number of kaon candidates within a 150 ns time window in KTAG; (b) Time difference between the kaon candidate closest to the track and the track itself as a function of particle momentum

The trigger request of hadronic energy suppressed the $K^+ \to \mu^+\nu$ decays by a factor larger than 50. A 75 GeV/c band can be observed, compatible with scattered beam particles reaching the straw spectrometer. These events are relatively enhanced by the hadronic energy requirement in the trigger. A kaon is defined by a five-fold coincidence of the KTAG, with about 90% efficiency. About 70% of the events have a kaon candidate within 150 ns from the track candidate (Fig. 53 (a)). The time difference between the kaon candidate closest in time to the track and the track itself as a function of the particle momentum clearly shows the accidental origin of the 75 GeV/c component (Fig. 53 (b)). An in-time kaon is defined as a kaon candidate in KTAG within $\pm$ 20 ns time window from the spectrometer track.

At least one coincidence between corresponding vertical and horizontal scintillator slabs in CHOD in time within $\pm$ 2 ns from the kaon candidate is further requested to clean the sample of tracks with a in-time kaon candidate. Fig. 54 shows the distribution of events without a kaon candidate (a) and with an in-time kaon candidate (b). The nature of the tracks of the events selected so far has been investigated using the RICH. About 98% of the events had at least a ring reconstructed, with a ring defined if at least 4 PMs' had fired, and about 35% more than 1 ring (Fig. 55 (a)). The position of the ring centre provides a measurement of the slope of the track independent from the spectrometer. Requirements on the track slopes measured with the RICH and the spectrometer have been applied to match a ring to a track. Fig. 55 (b) shows the ring radius as a function of the particle momentum for events with exactly one ring matched to a track. Pions and muons are clearly separated up to 30 GeV/c. The RICH resolution is not optimal at this stage of the analysis as the ring position was not corrected offline

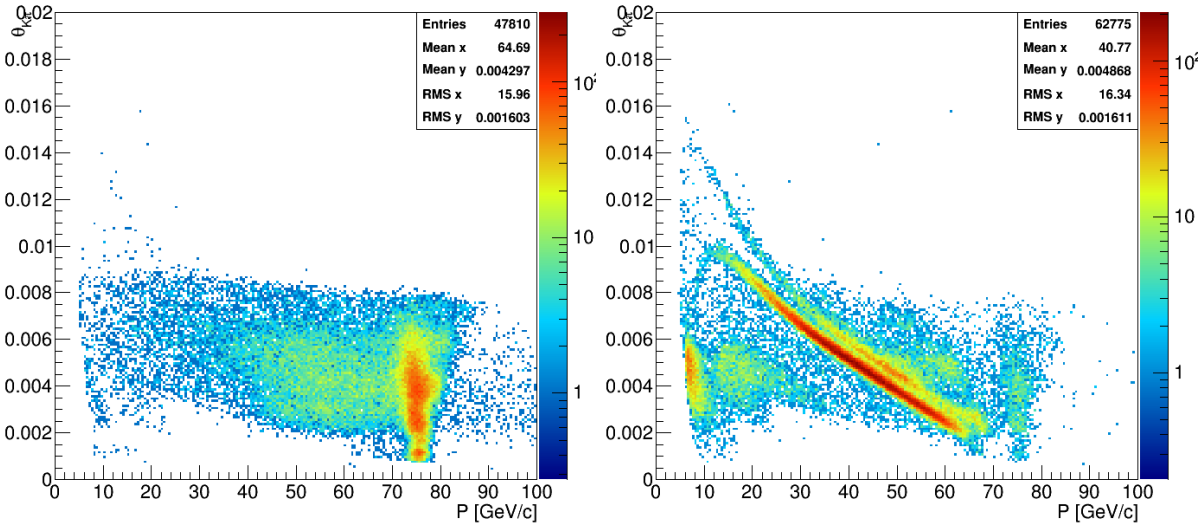

(a) (b)

Figure 54: Angle between the reconstructed track and the nominal kaon direction as a function of kaon momentum $[GeV/c]$ for (a) events without KTAG kaon candidate and (b) events with at least one in-time kaon candidate

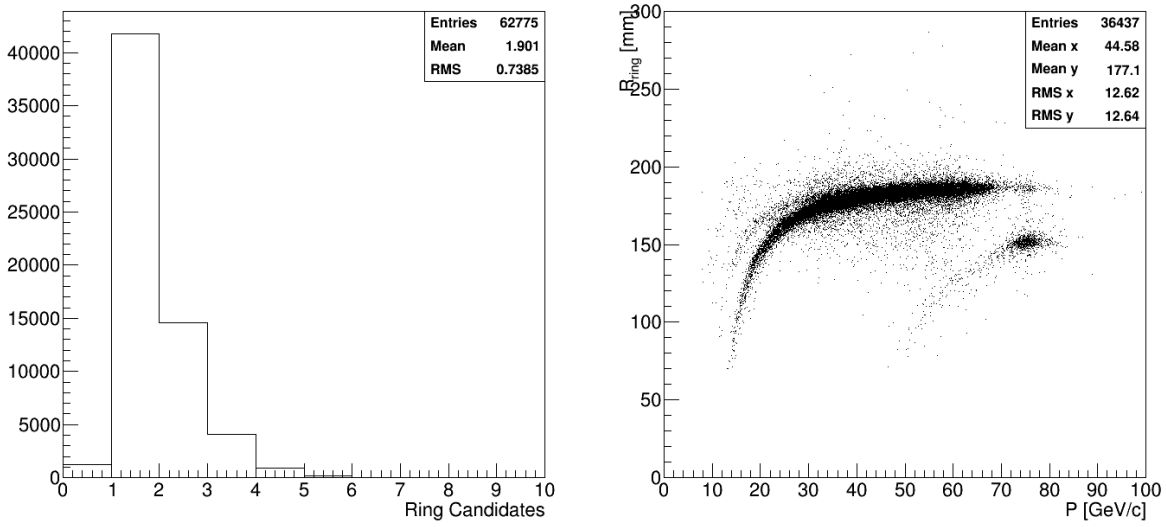

(a) (b)

Figure 55: (a) Number of ring per event reconstructed in the RICH; (b) radius of the ring as a function of the particle momentum for events with only one ring matched to the track

for mirror misalignment. A kaon component[3] is also present peaked at 75 GeV/c, while corresponding pions at 75 GeV/c are strongly suppressed by the KTAG requirement.

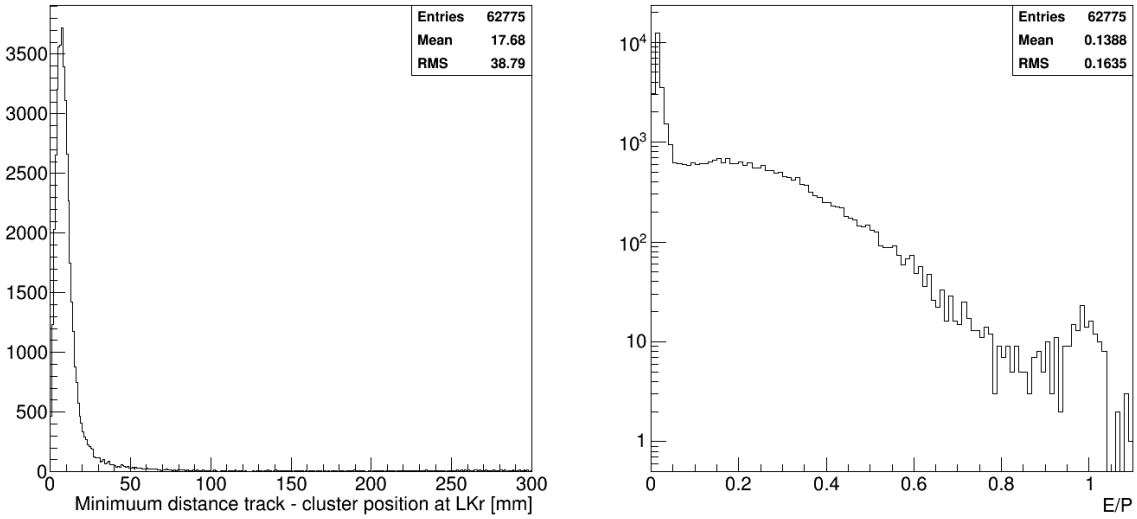

(a) (b)

Figure 56: (a) Distance between the track and the LKr cluster closest to the track; (b) Ratio between the energy of the cluster associated to a track and the particle momentum

In a similar way, the nature of the tracks of events with an in-time kaon has been investigated using the LKr. A cluster is associated to the track if closer than 10 cm to the position of the track extrapolated to the LKr surface. The distribution of the distance between the track and closest cluster shows a precise matching between clusters and tracks (Fig. 56 (a)). The ratio between the energy of the cluster matched to the track and the particle momentum is shown in Fig. 56 (b). The peak of mip clusters, the hadronic shoulder and a very tiny electron component around 1 are visible. The trigger condition requesting significant hadronic energy has strongly suppressed the electron component.

The origin of the track provides additional information on the nature of the events with a in-time kaon in Fig. 54 (b). For each event the origin of the track has been computed as the distance of closest approach between the track extrapolated backward in the region upstream of the straw spectrometer and the nominal kaon direction (Fig. 57). The Z coordinate is measured from the target position by convention. The final collimator at the beginning of the decay region extends from 100 to 102 m. GTK3 is located at 102.5 m. The CHANTI extends up to 103.5 m. The fiducial decay region starts at 105 m. The dipole magnets of the second achromat are located in the region upstream of 100 m. Because the origin of the track is computed assuming the direction of the beam after the achromat for kaons, a Z coordinate upstream of 100 m indicates an early origin of the track, but cannot be quantitatively related to physical elements along the beam line. Particles at 75 GeV/c come from scattering on GTK3 or on the final collimator. The region where to look for kaon decays extends from 105 to 165 m on Z

[3]A tiny component of scattered beam particles enters the acceptance providing a direct measurement of the beam composition

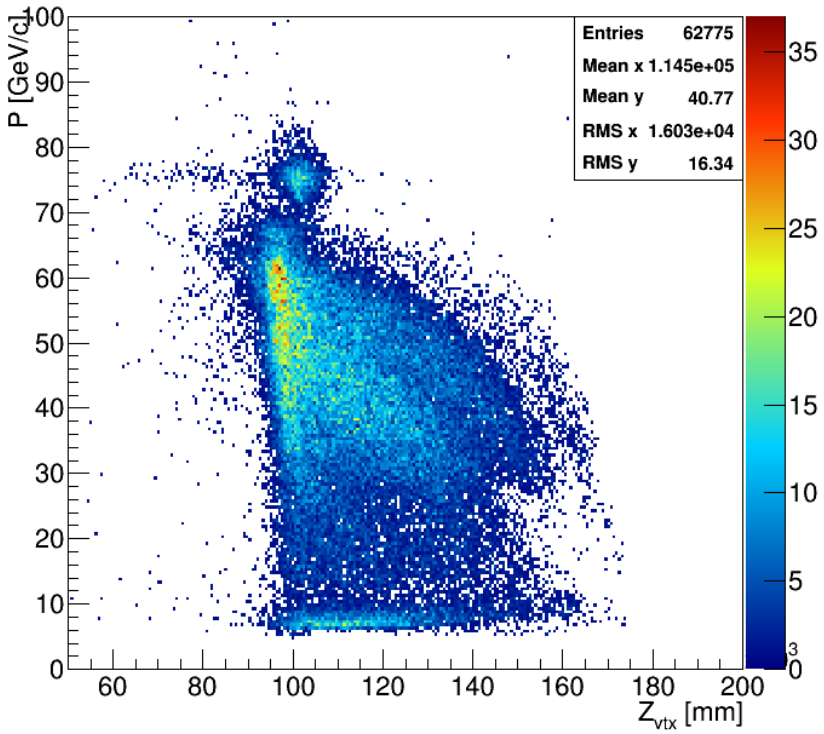

Figure 57: Particle momentum versus the Z coordinate of the closest distance of approach between the track and the nominal kaon direction

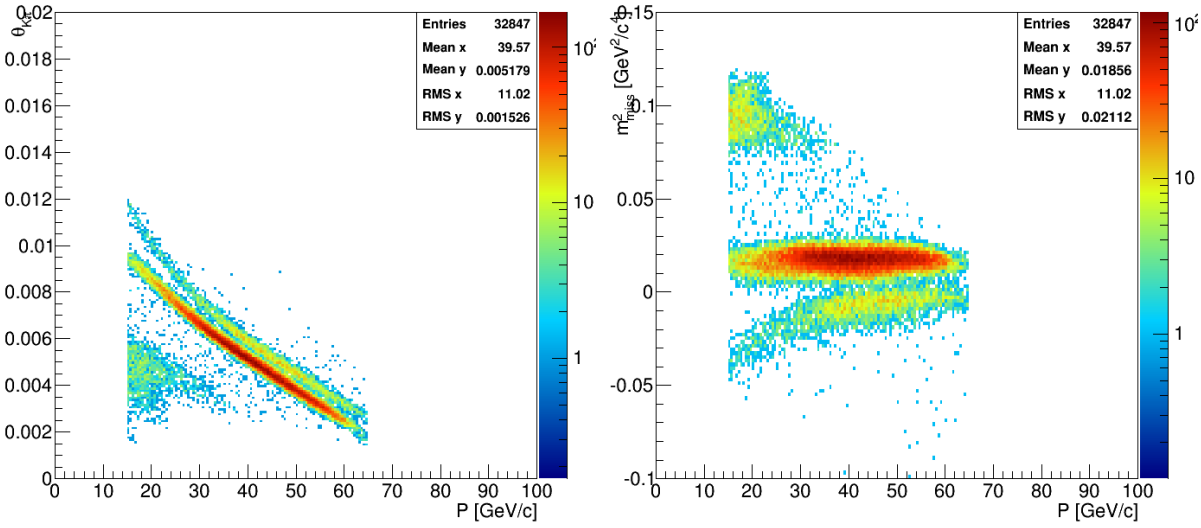

(a) (b)

Figure 58: (a) Angle between the reconstructed track and kaon nominal direction as a function of the track momentum $[GeV/c]$; (b) Squared missing mass as a function of particle momentum

and from 10 to 65 GeV/c in momentum. Events in this region are almost completely kaon decays, as suggested by the angle - momentum distribution for tracks satisfying the above requirements (Fig. 58 (a)).

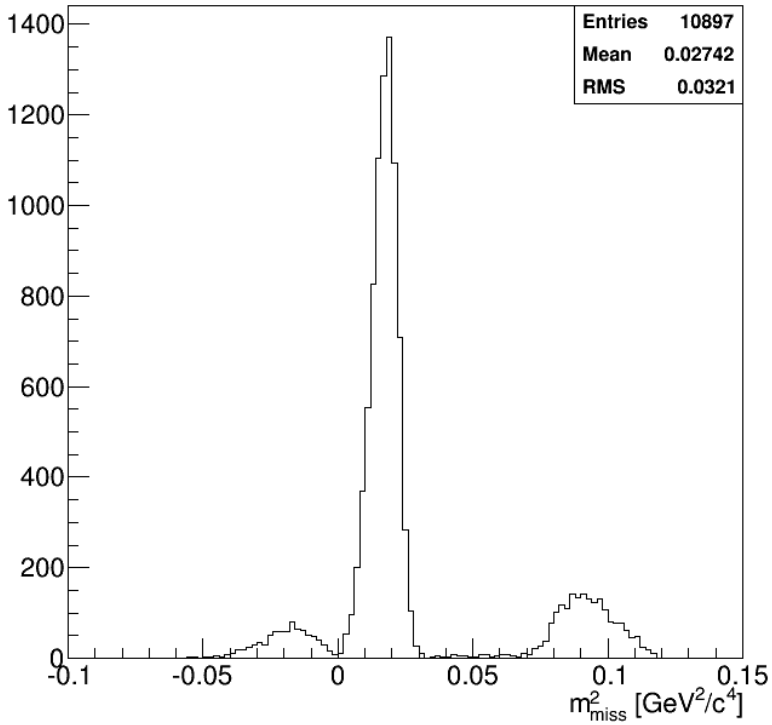

Figure 59: Squared missing mass distribution for single track events with momentum below 35 $GeV/$c

Fig. 58 (b) shows the distribution of the $m^2_{miss} = (P_K - P_\pi)^2$ as a function of the particle momentum, where P_π is the momentum of the particle under the π^+ hypothesis. $K^+ \to \pi^+\pi^0$ decays are distributed around the $m^2_{\pi^0}$ independently from the track momentum. $K^+ \to \mu^+\nu$ events lay on a band below zero depending on the momentum because of the pion mass assumption in the definition of m^2_{miss}, and approach the $K^+ \to \pi^+\pi^0$ events for increasing momenta. The $K^+ \to \pi^+\pi^+\pi^-$ and $K^+ \to \pi^+\pi^0\pi^0$ are visible on the top left corner of the plane for squared masses above $4m^2_{\pi^+}$. The standard signal region for $K^+ \to \pi^+\nu\bar{\nu}$ is defined to be:

- $15 < P_(\pi^+) < 35$ GeV/c;
- $0 < m^2_{miss} < 0.01$ GeV^2/c^4 (region 1);
- $0.026 < m^2_{miss} < 0.068$ GeV^2/c^4 (region 2).

The distribution of m^2_{miss} after the momentum cut is shown in Fig. 59. Region 2 lays between the peak of the $K^+ \to \pi^+\pi^0$ at $m_(\pi^0)^2$ and the 3-pion region above $4m^2_{\pi^+}$. Remaining events in region 2 come from kaon decays with photons, since photon rejection has not been applied in this analysis. Other contributions can be: kaon decays with electrons and resolution tails, possible at this stage of reconstruction. Region 1 lays between $K^+ \to \pi^+\pi^0$ and the $K^+ \to \mu^+\nu$. Events enter here from resolution tails. A factor four improvement in the resolution is expected after adding the GTK information.

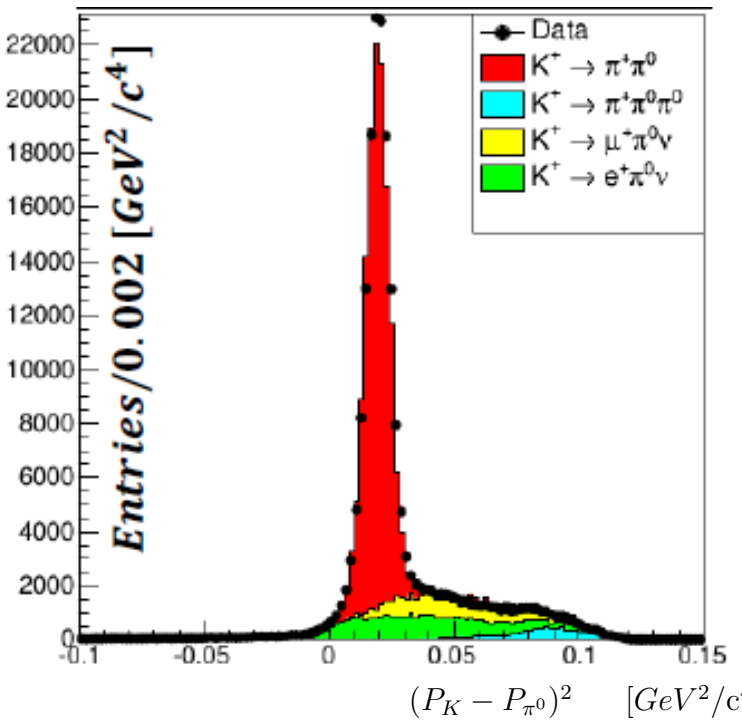

Figure 60: Squared missing mass for events passing the $K^+ \to \pi^+\pi^0$ selection

15.2 Selection of the main decay modes

Samples of the main kaon decay modes have been selected using data taken with a minimum bias trigger. The selection of $K^+ \to \pi^+\pi^0$, $K^+ \to \pi^+\pi^0\pi^0$ and $K^+ \to \pi^0 e^+\nu$ using only the LKr is briefly described in this section. Events with at least two electromagnetic clusters in the calorimeter have been selected. The Z coordinate of the kaon decay vertex can be computed from the distance and the energy of the clusters, assuming each pair of clusters coming from a π^0 decay. The three momentum of the π^0 is determined from the vertex and the cluster positions. Under the $K^+ \to \pi^+\pi^0$ hypothesis the momentum conservation constraint yields the π^+ three momentum, assuming the nominal momentum and direction for the kaon. A cluster in the LKr matched in position and time to the π^+ is further required in order to cleanly select the sample of $K^+ \to \pi^+\pi^0$. A peak in the $(P_K - P_{\pi^0})^2$ distribution corresponding to the $m^2_{\pi^+}$ identifies the $K^+ \to \pi^+\pi^0$ events. The $K^+ \to \pi^+\pi^0\pi^0$ selection requires the reconstruction of two π^0s' coming from the same vertex. The reconstruction of the π^+ follows as for the $K^+ \to \pi^+\pi^0$ selection. A peak in the $(P_K - P_{\pi^0_1} - P_{\pi^0_2})^2$ distribution corresponding to the $m^2_{\pi^+}$ tags the $K^+ \to \pi^+\pi^0\pi^0$ events. One π^0 plus another electromagnetic cluster are required for the $K^+ \to \pi^0 e^+\nu$ selection. The three momentum of the positron is computed assuming that this third cluster corresponds to the energy deposition of the positron. The momentum of the positron is taken to be equal to the energy of the cluster. The direction is computed from the cluster position, the coordinate of the decay vertex and the absolute value of the momentum to take into account the effect of the transverse momentum kick induced by the dipole magnet of the spectrometer. A peak at zero in the $(P_K - P_{\pi^0} - P_{e^+})^2$ identifies $K^+ \to \pi^0 e^+\nu$ events. Fig. 60, 61 and 62 show the distributions of the squared missing masses of the three selections described above. The corresponding distributions of the main kaon decay mode generated with the NA62 simulation are superimposed. The agreement between data and simulation is remarkable. The background under the

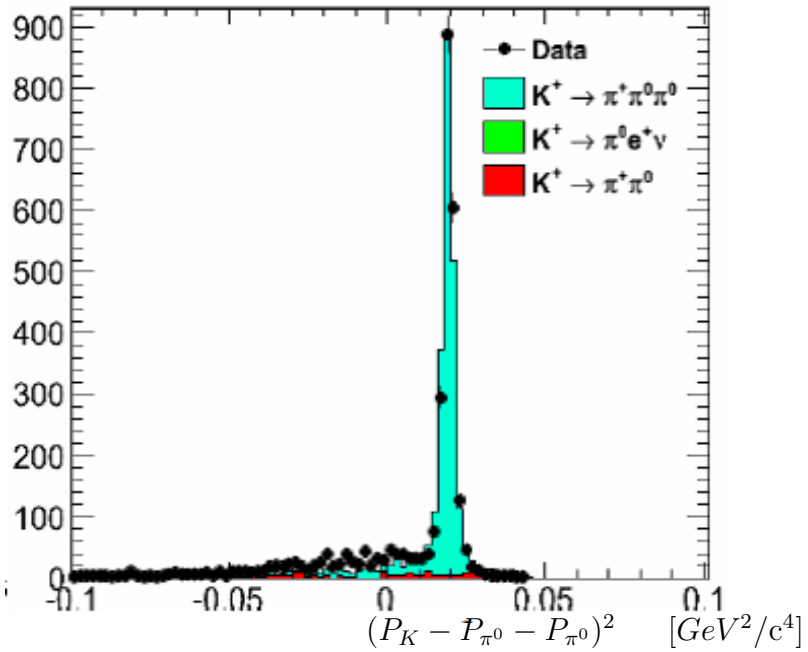

Figure 61: Squared missing mass for events passing the $K^+ \to \pi^+\pi^0\pi^0$ selection

signal peak is at the level or below one percent for all the selections. The $K^+ \to \pi^+\pi^0$ and $K^+ \to \pi^+\pi^0\pi^0$ events can be used to measure from data the kinematic rejection factor for the $K^+ \to \pi^+\nu\bar{\nu}$ analysis since the straw spectrometer is not used in the selection. The $K^+ \to \pi^0 e^+\nu$ events provide a pure sample of $\beta = 1$ particles for RICH studies.

16 Publications and analysis of older data

Since the last SPSC review in April 2014, the collaboration has completed two physics analyses based on data sets recorded in 2003 – 2004 by NA48/2.

The analysis of the rare decay mode $K^\pm \to \pi^0\pi^0 e^\pm\nu$ (BR $\sim 2 \times 10^{-5}$ with 18% precision) brings precise measurements of both Branching ratio (now 1.4% precision) and Form factor (now measured) and has been published in JHEP in August [17]. These results have already triggered theoretical interpretations in terms of isospin breaking and pion-pion re-scattering effects in the final state.

Following recent discussions about the possible existence of a *dark photon* to explain the muon $(g-2)$ measurement, a search for the dark photon A' has been conducted in the large π^0 sample accessible in kaon decays. The Dalitz decay of the $\pi^0 \to e^+e^-\gamma$ is a laboratory to look for $\pi^0 \to \gamma A'$ followed by $A' \to e^+e^-$ decay. Improved limits have been obtained in the mass range 9 to 70 MeV/c^2, ruling out the dark photon as an explanation for the muon $(g-2)$ measurement. A draft paper is under final review within the Collaboration and will be submitted as a CERN preprint before the end of March and then to a Journal [18].

More analyses of both NA62 and NA48/2 old data are still on-going: the high quality data recorded in former years are still valuable either to explore poorly known very rare kaon decays or to conduct high precision measurements. They are also an ideal practice for Master and PhD students, working on hardware-related subjects, as training for data analysis.

The above topics include:

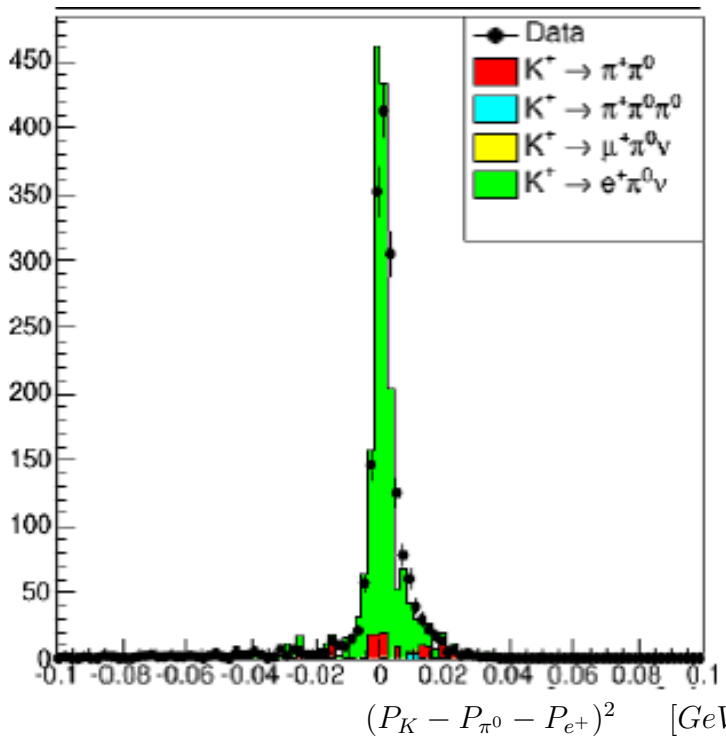

Figure 62: Squared missing mass for events passing the $K^+ \to \pi^0 e^+ \nu$ selection

- a measurement of the π^0 transition form factor (from a sample of $K^\pm \to \pi^\pm \pi^0_D$ with Dalitz decay);
- a search for long-lived sterile heavy neutrinos ν_H in the $50 - 350$ MeV/c^2 mass range produced in the $K^\pm \to \mu^\pm \nu_H$ decay;
- a precision study of $K^\pm \to \pi^0 l^\pm \nu$ form factors in both K_{e3} and $K_{\mu 3}$ modes,
- a search for lepton number violation in $K^\pm \to \pi^\mp \mu^\pm \mu^\pm$ decay;
- a first observation of the $K^\pm \to \pi^\pm \pi^0 e^+ e^-$ decay.
- a search for the rare and still unobserved $K^\pm \to \pi^0 \pi^0 \mu^\pm \nu$ mode;

The newer generation of students is now working on the NA62 data recorded last year and in the coming $2015 - 2018$ data taking runs.

The collaboration is actively contributing to major International Conferences and topical Workshops with NA62 Detector contributions and recently published or preliminary physics results from NA62 and NA48/2 data analyses. In the past year (April 2014 to April 2015), the collaboration speakers presented 41 talks and 3 posters to Physics Conferences and 10 talks and 3 posters to Instrumentation Conferences. More contributions are already foreseen in future 2015 Conferences.

References

[1] F. Hahn *et al*, NA62 Technical Design Document, NA62-10-07 (2010).

[2] A. J. Buras, D. Buttazzo, J. Girrbach-Noe and R. Knegjens, "Can we reach the Zeptouniverse with rare K and $B_{s,d}$ decays?," JHEP **1411** (2014) 121 [arXiv:1408.0728 [hep-ph]].

[3] G. Buchalla and A. J. Buras, "QCD corrections to rare K and B decays for arbitrary top quark mass," Nucl. Phys. B **400**, 225 (1993).

[4] M. Misiak and J. Urban, "QCD corrections to FCNC decays mediated by Z penguins and W boxes," Phys. Lett. B **451** (1999) 161 [hep-ph/9901278].

[5] G. Buchalla and A. J. Buras, "The rare decays K $\to$ pi neutrino anti-neutrino, B $\to$ X neutrino anti-neutrino and B $\to$ lepton+ lepton: An Update," Nucl. Phys. B **548** (1999) 309 [hep-ph/9901288].

[6] A. J. Buras, M. Gorbahn, U. Haisch and U. Nierste, "The Rare decay $K^+ \to \pi^+ \nu\bar{\nu}$ at the next-to-next-to-leading order in QCD," Phys. Rev. Lett. **95** (2005) 261805 [hep-ph/0508165].

[7] A. J. Buras, M. Gorbahn, U. Haisch and U. Nierste, "Charm quark contribution to $K^+ \to \pi^+ \nu\bar{\nu}$ at next-to-next-to-leading order," JHEP **0611** (2006) 002, [hep-ph/0603079].

[8] M. Gorbahn and U. Haisch, "Effective Hamiltonian for non-leptonic $|\Delta F| = 1$ decays at NNLO in QCD," Nucl. Phys. B **713** (2005) 291 [hep-ph/0411071].

[9] J. Brod and M. Gorbahn, "Electroweak Corrections to the Charm Quark Contribution to $K \to \pi\nu\bar{\nu}$," Phys. Rev. D **78** (2008) 034006 [arXiv:0805.4119 [hep-ph]].

[10] J. Brod, M. Gorbahn and E. Stamou, "Two-Loop Electroweak Corrections for the $K- > \pi\nu\bar{\nu}$ Decays," Phys. Rev. D **83** (2011) 034030 [arXiv:1009.0947 [hep-ph]].

[11] G. Buchalla and A. J. Buras, "Two loop large m (t) electroweak corrections to K $\to$ pi neutrino anti-neutrino for arbitrary Higgs boson mass," Phys. Rev. D **57** (1998) 216 [hep-ph/9707243].

[12] G. Isidori, F. Mescia and C. Smith, "Light-quark loops in K $\to$ pi nu anti-nu," Nucl. Phys. B **718** (2005) 319 [hep-ph/0503107].

[13] F. Mescia and C. Smith, "Improved estimates of rare K decay matrix-elements from Kl3 decays," Phys. Rev. D **76** (2007) 034017 [arXiv:0705.2025 [hep-ph]].

[14] A. J. Buras, D. Buttazzo, J. Girrbach-Noe and R. Knegjens, "$K^+ \to \pi^+ \nu\bar{\nu}$ and $K_L \to \pi^0 \nu\bar{\nu}$ in the Standard Model: Status and Perspectives," arXiv:1503.02693 [hep-ph].

[15] A. V. Artamonov *et al.* [BNL-E949 Collaboration], "Study of the decay $K^+ \to \pi^+ \nu\bar{\nu}$ in the momentum region $140 \leq \mathrm{P}(\pi) \leq 199$ MeV/c," Phys. Rev. **D79** (2009) 092004. [arXiv:0903.0030 [hep-ex]].

[16] The NA62 Experiment at CERN: status and perspectives, Giuseppe Ruggiero (CERN), `http://indico.cern.ch/event/360237/`

[17] J. Batley *et al.*, "Detailed study of the $K^{\pm} \to \pi^0\pi^0 e^{\pm}\nu$ (K^{00}_{e4}) decay properties", CERN-PH-EP-2014-145, arXiv:1406.4749 [hep-ex], JHEP **8** (2014) 159.

[18] J. Batley *et al.*, "Search for the dark photon in π^0 decays", draft review in progress.